

Separate and joint clustering characteristics of large Stokes number sprays subjected to moderately turbulent co-flows

Ali Rostami, Ri Li, and Sina Kheirkhah[†]

School of Engineering, University of British Columbia, Kelowna, British Columbia, Canada, V1V1V7

(Received xx; revised xx; accepted xx)

Separate and joint droplets, clusters, and voids characteristics of sprays injected in a turbulent co-flow are investigated experimentally. Simultaneous Mie scattering and Interferometric Laser Imaging for Droplet Sizing along with separate hotwire anemometry are performed. The turbulent co-flow characteristics are adjusted using zero, one, or two perforated plates. The Taylor length scale-based Reynolds number varies from 10 to 38, and the Stokes number estimated based on the Kolmogorov time scale varies from 3 to 25. The results show that the mean length scale of the clusters normalized by the Kolmogorov length scale varies linearly with the Stokes number. However, the mean void length scale is on the order of the integral length scale. It is shown that the number density of the droplets inside the clusters is about 10 times larger than that in the voids. The ratios of the droplets number densities in the clusters and voids to the total number density are independent of the test conditions and equal 8.3 and 0.7, respectively. The joint probability density function of the droplets diameter and clusters area shows that the droplets with the most probable diameter are found in the majority of the clusters. It is argued that intensifying the turbulence broadens the range of turbulent eddy size in the co-flow which allows for accommodating droplets with a broad range of diameters in the clusters. The results are of significance for engineering applications that aim to modify the clustering characteristics of large Stokes number droplets sprayed into turbulent co-flows.

Key words: Multiphase and particle-laden flows, Particle/fluid flow, Turbulent flows

1. Introduction

Turbulent particle-laden flows are of relevance to many engineering applications such as gas turbine engine combustors used for aircraft propulsion, cyclones utilized for particle separation, industrial driers, and slurry pumps, see Crowe *et al.* (2011); Kuerten (2016); Zhao *et al.* (2021). Thus, several theoretical, numerical, and experimental investigations have been carried out over the past decades, and many review papers have been published, see for example Poelma & Ooms (2006); Balachandar & Eaton (2010); Brandt & Coletti (2022). Review of these studies suggests that, among many non-dimensional parameters, the Stokes number (which is the ratio of particle to flow time scale, as defined in for example Crowe *et al.* (2011)) primarily influences the characteristics of the turbulent particle-laden flows. Although past investigations are of significant importance as they provide insight into relatively small and moderate Stokes number flows ($St \lesssim 10$), majority of industrial applications relevant to turbulent particle-laden flows corresponds to relatively large Stokes numbers ($St \gtrsim 10$). The present study is motivated by the need for understanding the spray

[†] Email address for correspondence: sina.kheirkhah@ubc.ca

characteristics at relatively large Stokes numbers. As elaborated in Baker *et al.* (2017) and Boddapati *et al.* (2020), the interaction of the particles and the background turbulent flow leads to the formation of regions with relatively large and small number of particles, which are referred to as clusters and voids, respectively, and are relevant to the present study. A brief review of the literature related to the clusters and voids is provided below.

The inertial bias and sweep-stick mechanisms are proposed in the literature to elaborate the formation of clusters and voids in turbulent flows. The former suggests that during a particle and eddy interaction, the large eddies centrifuge out the particles and accumulate them in regions that feature small vorticities and large strain rates, as explained in Maxey (1987); Squires & Eaton (1991); Wang & Maxey (1993). Compared to the inertial bias mechanism, the sweep-stick mechanism suggests that the vorticity and strain rate fields may not be sufficient in explaining the positioning of the particles and hence formation of the clusters, see Goto & Vassilicos (2008). The sweep-stick mechanism suggests that particles with $St \gtrsim 1$ tend to be positioned in the spatial locations with zero acceleration. Then, these particles are carried by large eddies in the flow, see Goto & Vassilicos (2006); Monchaux *et al.* (2012); Mora *et al.* (2021); Hassaini & Coletti (2022).

Various tools and methods have been developed to identify the clusters and voids from the spatial distribution of the particles. For example, Monchaux *et al.* (2010), Tagawa *et al.* (2012); Frankel *et al.* (2016) utilized the Voronoï cells, Andrade *et al.* (2022) used the combined graph and Voronoï cells, Fessler *et al.* (1994) and Villafañe-Roca *et al.* (2016) implemented the box-counting method, and Salazar *et al.* (2008); Saw *et al.* (2008); Sahu *et al.* (2016) applied the radial distribution functions to identify the clusters. The Voronoï cells (relevant to the present investigation) can allow for estimating the degree of clustering, which is defined (see for example Boddapati *et al.* (2020)) as the root mean square (RMS) of the Voronoï cells area (σ) divided by that if the droplets were distributed following a Random Poisson Process (RPP), σ_{RPP} , minus unity. Studies of Reade & Collins (2000); Aliseda *et al.* (2002); Yang & Shy (2005); Monchaux *et al.* (2010); Obligado *et al.* (2014); Sumbekova *et al.* (2017) show that the degree of clustering is influenced by three non-dimensional parameters that are the Stokes number (St) estimated based on the Kolmogorov time scale, Taylor length scale-based Reynolds number (Re_λ), and the droplets volume fraction (ϕ_v). Reade & Collins (2000); Aliseda *et al.* (2002); Yang & Shy (2005); Monchaux *et al.* (2010); Obligado *et al.* (2014) showed that the degree of clustering increases by increasing the Stokes number and maximizes at $St \approx 1$. Sumbekova *et al.* (2017) proposed a power-law correlation between the degree of clustering and St , Re_λ , and ϕ_v . Compared to Reade & Collins (2000); Aliseda *et al.* (2002); Yang & Shy (2005); Monchaux *et al.* (2010); Obligado *et al.* (2014), the study of Sumbekova *et al.* (2017) showed that St does not greatly influence the degree of clustering, however, this parameter scales with Re_λ and the square root of ϕ_v .

Few experimental studies, see Zimmer *et al.* (2003) and Jedelsky *et al.* (2018), were carried out to quantify the position of the clusters and voids in turbulent spray flows. Their results show that the clusters are formed in the central region of the sprays, where small size droplets are located. Studies of Sumbekova *et al.* (2017); Obligado *et al.* (2014); Monchaux *et al.* (2010) showed that the Probability Density Function (PDF) of the cluster and void areas feature power-law correlations with the exponents of the power-law ranging from about -1.5 to -2.1 and -1.7 to -1.9, respectively. Sumbekova *et al.* (2017) showed that the PDFs of the cluster and void areas normalized by their corresponding mean value feature a power-law decay with an exponent of -5/3 for normalized cluster and void areas ranging from about 0.2 to 10.

In addition to the positions and the PDFs of the cluster and void areas, the length scale of the clusters and voids can be used to understand their relations with the length scale of the turbulent flow. The characteristic length scale of the clusters and voids are defined as

the square root of the cluster and void mean areas, respectively. Studies of Aliseda *et al.* (2002); Obligado *et al.* (2014); Sumbekova *et al.* (2017); Sahu *et al.* (2016); Boddapati *et al.* (2020) showed that the cluster length scale is about 5–90 times the Kolmogorov length scale. For voids, Sumbekova *et al.* (2017) showed that the length scale can increase to about 200 times the Kolmogorov length scale. Power-law formulations were developed in Sumbekova *et al.* (2017), and it was shown that the normalized cluster length scale is proportional to $St^{-0.25} Re_\lambda^{4.7} \phi_v^{1.2}$. Also, Sumbekova *et al.* (2017) showed that, despite the Stokes number does not significantly influence the normalized voids length scale, this positively relates to Re_λ and ϕ_v .

Although the generated knowledge from the particle-laden flow studies (with a brief review presented above) is of significant importance, as it allows to understand the clustering characteristics of droplets corresponding to relatively small Stokes numbers ($St < 10$), many engineering applications feature droplets with large Stokes numbers. In such applications, it is of significant importance to understand the distribution of the droplet diameter and their number density within a given cluster and for $St > 10$. For example, for spray combustion-related applications (which feature Stokes numbers in excess of 10), the mean distance between the fuel droplets and their number density within a given cluster can influence the droplets evaporation rate as well as the flame location and the temperature distribution, see for example Sahu *et al.* (2018); Hardalupas *et al.* (1994); Akamatsu *et al.* (1996); Pandurangan & Sahu (2022). The objective of the present study is to investigate the effect of the Stokes number on both the geometrical (e.g. clusters and voids length scales) as well as the joint characteristics of the droplets and clusters/voids for $St > 10$. In the following, the methodology, data reduction, results, and concluding remarks are presented in Sections 2–5, respectively.

2. Experimental methodology

The experimental setup, the utilized diagnostics, and the tested conditions are presented in this section.

2.1. Experimental setup

The experimental setup consists of a liquid delivery and flow apparatuses, which are shown in Fig. 1 as items (1–3) and item (4), respectively. A nitrogen bottle, item (1), in the figure as well as a dual-valve MCRH 2000 ALICAT pressure controller, item (2), were used to purge water inside a pressure vessel, item (3). Then, water flowed into the flow apparatus, see the blue arrow in Fig. 1. In addition to water, a compressor was used to provide air into the flow apparatus, see the black arrow in Fig. 1. The air flow rate was controlled using an MCRH 5000 ALICAT mass flow controller.

The flow apparatus is composed of a diffuser section (with an area ratio of 4), a settling chamber (which is equipped with 5 equally spaced mesh screens), a contraction section (with an area ratio of 7), and a nozzle (with an inner diameter of 48.4 mm). Further details regarding the apparatus can be found in Mohammadnejad *et al.* (2022); Kheirkhah & Gülder (2015); Kheirkhah (2016). The nozzle section of the flow apparatus is shown in Fig. 2. In the present study, this section was modified to allow for producing a spray subjected to turbulent co-flow of air. The nozzle includes a 6.4 mm outer diameter tube (which carries water), a spray injector, a turbulence generation mechanism, and a ring-shaped tube-holder, which was press-fit against the inner wall of the nozzle and supported the tube vertically using 4 bars and a collar. The injector was a pressure swirl atomizer from Delavan (model 6330609), which produced a polydisperse spray. The spray flow rate depends on the vessel pressure, and

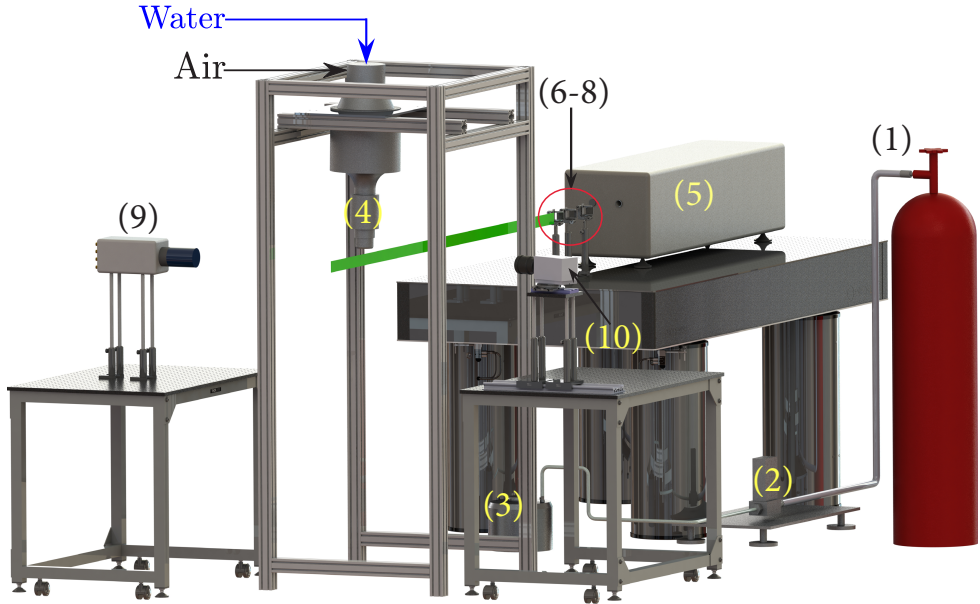


Figure 1. The experimental setup. (1–3) are a nitrogen bottle, a pressure controller, and a pressurized water vessel. (4) is the nozzle section of the flow apparatus. (5) is a 532 nm Nd:YAG laser. (6–8) are the laser sheet forming optics and optomechanics. (9) and (10) are a Nova S12 camera and lens as well as a Zyla camera and lens for simultaneous shadowgraphy and ILIDS measurements.

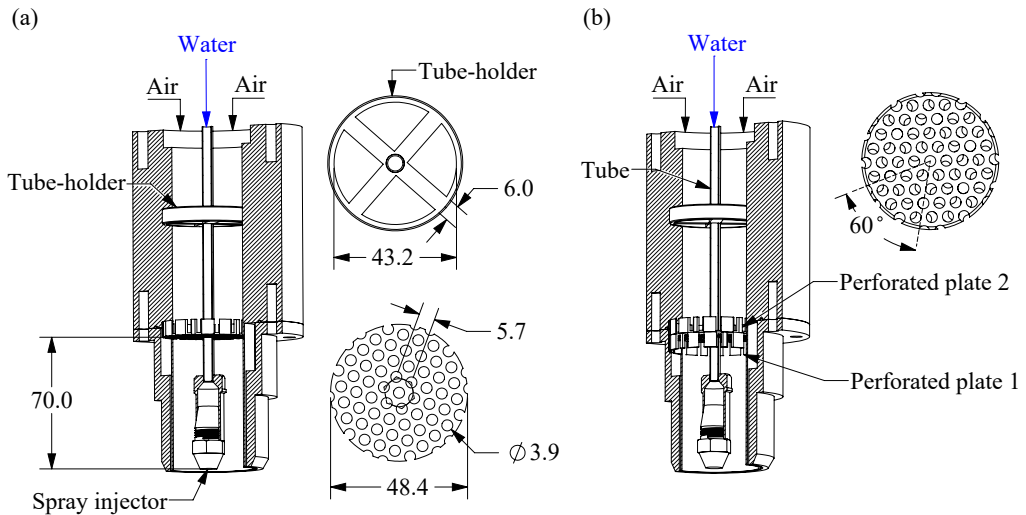


Figure 2. (a) and (b) are the 3D drawings of the flow apparatus nozzle section for the second and third turbulence generation mechanisms, respectively.

separate calibration experiments were performed to obtain the relation between the vessel pressure and the spray flow rate, as discussed in Appendix A.

Three turbulence generation mechanisms were used in the present study. Either no perforated plate, one perforate plate (see Fig. 2(a)), or two perforated plates attached back-to-back (see Fig. 2(b)) were utilized. The outer diameter of each perforated plates is 48.4 mm,

matching the inner diameter of the nozzle. Each perforated plate features 3.9 mm diameter holes arranged in a hexagonal pattern. For the first turbulence generation mechanism, the perforated plates in Fig. 2 were removed. For the third turbulence generation mechanism, the plates were rotated by 60° with respect to one another, similar to Kheirkhah & Gülder (2014). For the second turbulence generation mechanism, the planes containing the holes; and, for the third turbulence generation mechanism, the center plane of the two perforated plates were positioned 76.0 mm upstream of the nozzle exit plane, similar to the studies of Kheirkhah & Gülder (2015) and Kheirkhah (2016).

2.2. Diagnostics

Separate hotwire anemometry (HWA) as well as simultaneous Mie scattering and Interferometric Laser Imaging for Droplet Sizing (ILIDS) were performed. The hotwire anemometry was used to characterize the background turbulent flow. A schematic of the diagnostics used in the present study is shown in Fig. 1. The hardware configuration for the HWA is identical to that used in Mohammadnejad *et al.* (2022); and, a separate illustration is not presented in Fig. 1. For all test conditions, the HWA data was acquired at a frequency of 100 kHz and for 90 s, corresponding to 9,000,000 data points. The simultaneous Mie scattering and ILIDS images were collected at a frequency of 10 Hz and for a duration of 100 s, corresponding to 1000 image pairs. Further details regarding the HWA, Mie scattering, and ILIDS diagnostics are provided in the following.

2.2.1. Hotwire anemometry

The hardware of the HWA system consists of a probe (model 55P01 from Dantec), a probe support (model 9055H0261 from Dantec), and two motorized translational stages (MTS50-Z8 from Thorlabs). The probe is a single wire sensor, which is 3 mm long (with an active sensor length of 1.25 mm) and has a diameter of $5 \mu\text{m}$. A mini-constant temperature anemometry (mini-CTA) circuit (model 9054T0421 from Dantec) maintains the wire temperature, with an overheat ratio of 0.7. The motorized translational stages featured a 50 mm range of operation, which was sufficient for the present study. Further details regarding the HWA system as well as the calibration procedure can be found in Mohammadnejad *et al.* (2022).

A Cartesian coordinate system was used in the present investigation. The origin of the coordinate system is at the exit plane of the nozzle section and at the nozzle centerline, as shown in Fig. 3. The z -axis coincides with the nozzle centerline. The x -axis is normal to the z -axis and is parallel with the laser sheet shown in Fig. 1. The HWA was performed at $z = 35.0$ mm and at horizontal locations spaced by 5.0 mm along the x -axis, ranging from $x = -20.0$ mm to 20.0 mm as shown as the red cross data symbols in Fig. 3.

2.2.2. Mie scattering

The Mie Scattering hardware consists of a pulsed Nd:YAG laser (Lab-Series-170 from Spectra Physics, shown by item (5) in Fig. 1), the sheet forming optics (see, items (6–8)), and a camera equipped with collection optics (item (9)). The laser produces a 1064 nm beam, which is converted to a 532 nm beam using a harmonic generator. The laser was operated at a reduced (compared to its maximum) but fixed energy in order to avoid saturation in the collected Mie scattering images. The laser beam was 8.0 mm in diameter, which was converted to a 40 mm high and 1 mm thick laser sheet using a plano-concave cylindrical lens with a focal length of -100 mm, a plano-convex cylindrical lens with a focal length of 500 mm, and a cylindrical lens with a focal length of 1000 mm, see items (6–8) in Fig. 1. The centerline of the collimated laser sheet was positioned at $z = 55.0$ mm. The Mie scattering images were acquired using a Photron Fastcam Nova S12 camera equipped with a Macro

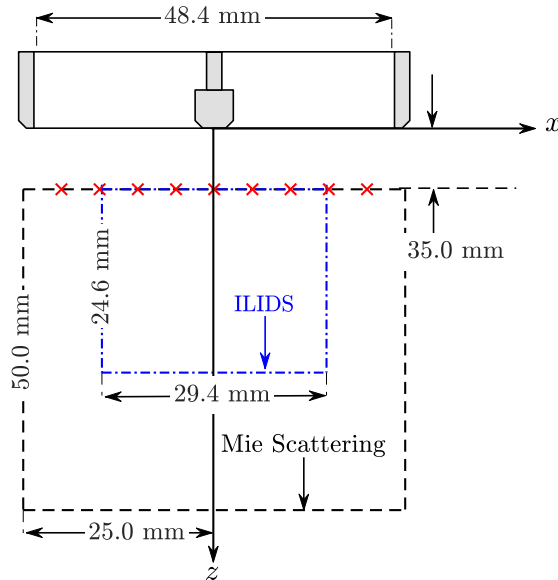


Figure 3. The coordinate system and the measurements locations. The red cross data points present the locations at which the hotwire anemometry was performed. The dashed black and dotted dashed blue squares are the regions of interest for the Mie scattering and ILIDS measurements, respectively. The minimum vertical distance for the above measurements is 35.0 mm from the nozzle exit plane, and this distance shown in the figure is not to scale.

Sigma lens, which had a focal length of $f = 105$ mm and its aperture size was set to $f/2.8$. A bandpass filter with a center wavelength and Full Width at Half Maximum of 532 and 20 nm was mounted on the camera lens. By adjusting the working distance of the camera, a field of view of 70.0 mm along x -axis and 70.0 mm along the z -axis was obtained, which corresponds to a pixel resolution of $70 \text{ mm}/1024 \text{ pixels} = 68 \text{ } \mu\text{m}/\text{pixel}$. For analysis and presentation purposes, the above field of view was cropped to a $50.0 \text{ mm} \times 50.0 \text{ mm}$ square, which is shown by the black dashed box in Fig. 3.

2.2.3. Interferometric Laser Imaging for Droplet Sizing

The Interferometric Laser Imaging for Droplet Sizing was performed to measure the droplets diameter, similar to Qieni *et al.* (2016); Bocanegra Evans *et al.* (2015); Garcia-Magarino *et al.* (2021). In ILIDS, the droplet diameter is measured by analyzing the interference pattern of the reflected and first-order refracted rays scattered from spherical droplets that are illuminated by a laser. The ILIDS hardware includes the laser and the laser-sheet forming optics, see items (5–8) in Fig. 1, which are identical to those used for the Mie scattering technique as well as an sCMOS camera equipped with a Macro sigma lens ($f = 105$ mm and aperture size of $f/2.8$) and a high-precision rotary stage, see item (10). The camera is a 5.5 Zyla from Andore, which has a $2560 \text{ pixels} \times 2160 \text{ pixels}$ sensor. The ILIDS field of view was 29.4 mm along the x -axis and 24.6 mm along the z -axis, which led to a pixel resolution of $29.4 \text{ mm}/2560 \text{ pixels} = 11.4 \text{ } \mu\text{m}/\text{pixel}$. Using the rotary stage, the orientation of the camera and lens was adjusted with respect to the direction of the laser sheet. Specifically, the angle between the lens centerline and the laser sheet, referred to as θ , was set to 69° as per the recommendation of Sahu *et al.* (2016). It was confirmed this angle provided the best clarity of the fringe patterns. Finally, the formulation in Hayashi *et al.* (2012) and Thimothee *et al.* (2016) was used to estimate the droplet diameter, which is given by

$$d = \frac{2\lambda_L N}{\alpha} \left[\cos\left(\frac{\theta}{2}\right) + \frac{m \sin\left(\frac{\theta}{2}\right)}{\sqrt{m^2 - 2m \cos\left(\frac{\theta}{2}\right) + 1}} \right]^{-1}, \quad (2.1)$$

where λ_L is the wavelength of the laser and is 532 nm. In Eq. (2.1), m is the droplets index of refraction, which equals 1.33 for water, and α is the collection angle of the scattered light. This angle depends on the utilized lens diameter (d_l) and the distance between the camera lens and the laser sheet (c). The collection angle is calculated using $\alpha = 2 \arctan[d_l/(2c)]$. In Eq. (2.1), N is the number of the fringe patterns and is estimated using the procedure discussed in the next section. Since the viewing angle of the ILIDS camera is different than that of the Mie scattering camera, a discrepancy exists in estimating the location of the droplets using the Mie scattering and ILIDS techniques. Such discrepancy needs to be addressed for estimating the joint characteristics of the droplets and clusters/voids. This discrepancy was addressed by registering the Mie scattering images onto the ILIDS images, with details discussed in Appendix B.

2.3. Test conditions

In total, 13 experimental conditions were tested, with the corresponding details tabulated in Table 1. The first row in the table highlights the test condition for which no co-flow is utilized and the spray is issued into the quiescent air. The first column in the table presents the utilized turbulence generation (TG) mechanism, with OPP, 1PP, and 2PP referring to zero, one, and two perforated plates, respectively. For each turbulence generation mechanism, the mean bulk flow velocities of 3.5, 7.0, 10.5, and 14.0 m/s were tested. The root-mean-square (RMS) of the streamwise velocity (u'_0) and the integral length scale (Λ) estimated at $x = 0$ mm and $z = 35.0$ mm are listed in the third and fourth columns of Table 1, respectively. The integral length scale was calculated using the Taylor's frozen turbulence hypothesis, see Taylor (1938), and following the procedure detailed in Mohammadnejad *et al.* (2022). Specifically, the integral length scale was calculated as the multiplication of the mean bulk flow velocity and the integral of the streamwise velocity auto-correlation from $t = 0$ to the first time that the auto-correlation becomes zero. The Taylor (λ) and Kolmogorov (η) length scales were calculated using $\lambda = \Lambda(u'_0 \Lambda / \nu)^{-0.5}$ and $\eta = \Lambda(u'_0 \Lambda / \nu)^{-0.75}$, with ν being the air kinematic viscosity estimated at the laboratory temperature. The values of λ and η are tabulated in the fifth and sixth columns of Table 1. For all test conditions, the most probable droplet diameters (d^*) were obtained using the ILIDS diagnostic and are listed in the seventh column of the table. Further details regarding the size distribution of the droplets are discussed in subsection 4.1.

The Taylor length scale-based Reynolds number, the Stokes number, and the liquid volume fraction are non-dimensional parameters that can potentially influence the interaction of the droplets with the background turbulent flow. The Taylor length scale based-Reynolds number was estimated using $Re_\lambda = u'_0 \lambda / \nu$; and, henceforth, for brevity, Re_λ is referred to as the Reynolds number, with the corresponding values listed in the eighth column of Table 1. In the present study, Re_λ varies from about 10 to 36, which corresponds to relatively moderate values. Following Reade & Collins (2000), the Stokes number was calculated using

$$St = \frac{1}{18} \frac{\rho_W}{\rho_A} \left(\frac{d}{\eta}\right)^2 \quad (2.2)$$

where ρ_W and ρ_A are the water and air densities, respectively, both estimated at the laboratory temperature. In Eq. (2.2), d is the droplet diameter. In the present study, d was taken as the most probable droplet diameter for estimation of the Stokes number. The values of St are

TG	U (m/s)	u'_0 (m/s)	Λ (mm)	λ (mm)	η (μm)	d^* (μm)	Re_λ	St	ϕ_v ($\times 10^6$)
N.A.	0.0	N.A.	N.A.	N.A.	N.A.	34	N.A.	N.A.	1.8
OPP	3.5	0.57	5.9	0.39	102	29	14.9	4.5	1.8
OPP	7.0	1.07	5.8	0.29	63	29	20.3	11.4	1.2
OPP	10.5	1.55	7.1	0.26	50	29	27.1	18.5	1.0
OPP	14	2.14	10.0	0.26	43	29	37.8	25.3	1.1
1PP	3.5	0.4	4.0	0.39	121	29	10.3	3.2	2.1
1PP	7.0	0.85	4.7	0.29	71	29	16.3	9.2	1.6
1PP	10.5	1.22	4.7	0.24	54	29	19.5	15.9	1.4
1PP	14.0	1.63	5.0	0.21	44	28	23.3	21.4	1.2
2PP	3.5	0.64	4.9	0.34	89	29	14.5	5.7	2.2
2PP	7.0	1.35	5.9	0.26	53	29	23.0	16.5	1.6
2PP	10.5	1.55	7.3	0.27	51	29	27.5	18.3	1.3
2PP	14.0	1.93	10.0	0.28	47	28	35.9	20.2	1.2

Table 1. Test conditions.

tabulated in Table 1 and range from about 3 to 25, which are relatively large compared to those of the studies that were performed in multi-phase wind tunnels. Following the definition provided in Elghobashi (1994), the liquid volume fraction was calculated from

$$\phi_v = n \frac{V_d}{V_{\text{ROI}}}, \quad (2.3)$$

where n is the mean number of droplets within the volume of the region of interest, V_{ROI} . In Eq. (2.3), V_d is the droplet volume. For each test condition, n was estimated using the Mie scattering technique and averaged over all collected Mie scattering images. $V_{\text{ROI}} = 50 \times 50 \times 1 \text{ mm}^3$ and $V_d = (\pi/6)d^{*3}$. The values of ϕ_v are listed in the last column of Table 1 and change from about 1×10^{-6} to 2×10^{-6} . Following Elghobashi (1994), the estimated liquid volume fractions are relatively small, rendering the tested sprays as dilute. In essence, compared to past studies, the non-dimensional parameters of the present study correspond to dilute sprays with moderate Reynolds but large Stokes numbers.

For all test conditions with the co-flow, St , Re_λ , and ϕ_v vary by changing the mean bulk flow velocity and the turbulence generation mechanism. Variations of St versus U , Re_λ versus St , and ϕ_v versus St are presented in Figs. 4(a–c), respectively. As can be seen, the variations of these non-dimensional parameters are mostly influenced by the mean bulk flow velocity. That is increasing U increases St and Re_λ but decreases ϕ_v . It is important to note that, in the present study, changing the turbulence generation mechanism for a fixed value of U and changing U for a given turbulence generation mechanism both change the background RMS velocity fluctuations, which changes St , Re_λ , and ϕ_v . In the following sections, when possible, comparisons are made at fixed values of Reynolds number but varying Stokes number and vice versa.

3. Data Reduction

Of prime importance to the present study are identifications of clusters and voids as well as estimating the droplets diameter. The former and the later are obtained using the Mie scattering and the Interferometric Laser Imaging for Droplet Sizing, respectively, with details provided in the following subsections.

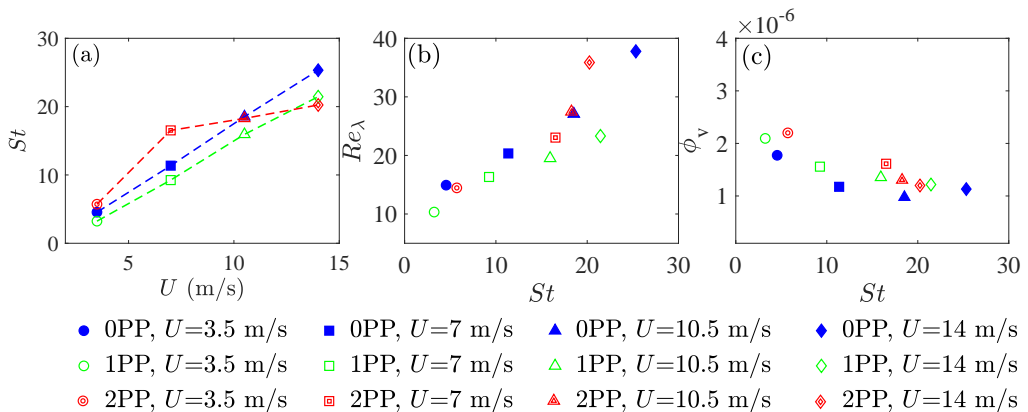


Figure 4. Variations of (a) the Stokes number versus mean bulk flow velocity, (b) the Taylor length scale-based Reynolds number versus Stokes number, and (c) the liquid volume fraction versus the Stokes number. The blue, green, and red colors correspond to turbulence generation mechanisms with zero, one, and two perforated plates, respectively.

3.1. Clusters and voids identification

The procedures followed to identify the clusters and voids are illustrated in Fig. 5. A representative raw Mie scattering image corresponding to the no co-flow test condition is shown in Fig. 5(a). The results in Fig. 5(a) were binarized to identify the centers of the droplets, which are shown by the black circular data points in Fig. 5(b). It is important to note that the laser intensity features a nearly top-hat profile in the region of interest. Also, the Mie scattering background field (averaged over 1000 images taken with the camera lens capped) is about 0.2% of the maximum acquired intensity. Thus, normalizing the Mie scattering images by the spatially varying laser intensity as well as subtracting the background field from the Mie scattering images did not influence the process for identifying the droplets centers in Fig. 5(b). Using the centers of the droplets along with the “voronoi” function in MATLAB, the Voronoi cells around each droplet were obtained and overlaid on Fig. 5(b) using the black lines.

The probability density function of the Voronoi cells area (A) normalized by their mean area (\bar{A}) was calculated using all Mie scattering images of the no co-flow test condition, and the resultant PDF is presented in Fig. 5(c) with the black circular data points. Provided the droplets spatial distribution followed the Random Poisson Process (RPP), the PDF of A/\bar{A} , referred to as PDF_{RPP} , could be estimated using that in Ferenc & Néda (2007) which is given by

$$PDF_{RPP} = \frac{b^a}{\Gamma(a)} \left(\frac{A}{\bar{A}} \right)^{a-1} \exp(-bA/\bar{A}). \quad (3.1)$$

In Eq. (3.1), a and b are fitting parameters with $a = b = 3.5$, and Γ is the gamma-function with $\Gamma(a) = 3.32$. The variation of PDF_{RPP} versus A/\bar{A} was obtained and presented by the black solid curve in Fig. 5(c). Additionally, using MATLAB, 1000 images were synthetically generated by distributing particles inside the domain of investigation randomly, with the number of droplets identical to that shown in Fig. 5(a), and the PDF of A/\bar{A} was calculated. It was confirmed that the PDF of the Voronoi cells normalized area for randomly distributed particles closely follows the right-hand-side of Eq. (3.1). Next, the intersections of PDF_{RPP} and the $PDF(A/\bar{A})$ for the results in Fig. 5 were obtained, which are shown by the dashed

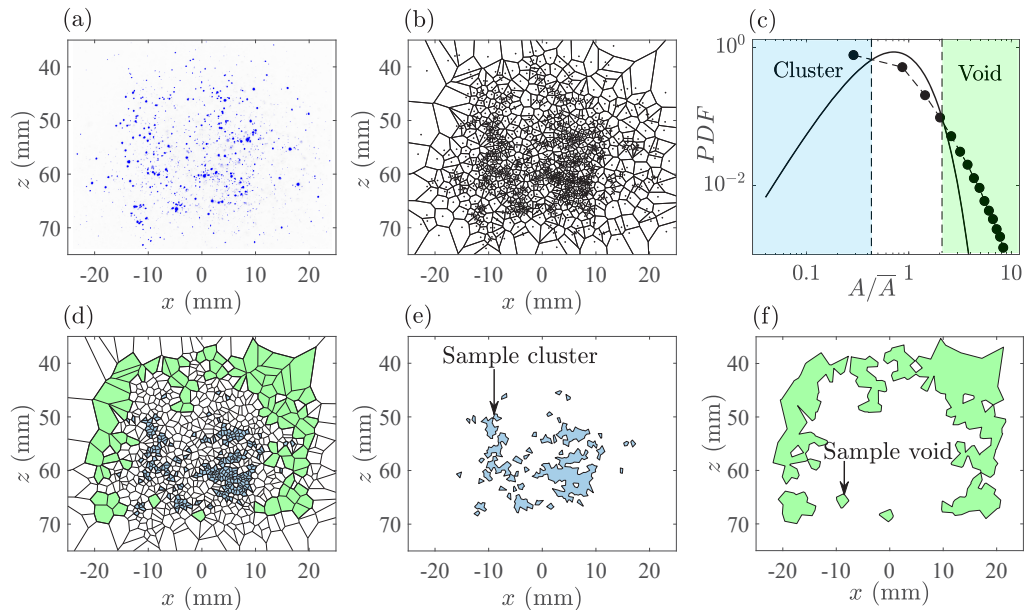


Figure 5. (a) Representative raw Mie scattering image corresponding to the no co-flow test condition. (b) Centers of the droplets in (a) and the Voronoi cells. (c) PDF of the Voronoi cells areas normalized by their mean. Overlaid in (c) is the PDF_{RPP} from Eq. (3.1). The dashed lines in (c) are $A/\bar{A} = 0.5$ and 2.2 . (d) presents the cells with areas related to clusters (blue cells) and voids (green cells). (e) and (f) are the clusters and voids corresponding to the Mie scattering image in (a), respectively.

lines corresponding to $A/\bar{A} = 0.5$ and 2.2 . The Voronoi cells with area smaller than $0.5\bar{A}$ were labeled as clusters, and Voronoi cells with area larger than $2.2\bar{A}$ were labeled as voids. The identified clusters and voids corresponding to the Mie scattering image in Fig. 5(a) are shown by the blue and green color cells in Fig. 5(d). As can be seen, clusters or voids may feature connected boundaries forming larger clusters and voids. Following Andrade *et al.* (2022), in the present study, the graph theory was used to identify and group the clusters/voids cells that are interconnected. For the results presented in Fig. 5(d), the identified clusters and voids are separately shown in Figs. 5(e) and (f), respectively. These clusters and voids were used for further analysis in Section 4.

3.2. Droplets location and diameter estimation

The ILIDS images were reduced to estimate the droplets location and diameters. A summary of the processes followed to reduce the ILIDS images is illustrated in Fig. 6. A representative raw ILIDS image is shown in Fig. 6(a), which corresponds to the test condition with two perforated plates and the mean bulk flow velocity of 14.0 m/s. Following the procedure used in Bocanegra Evans *et al.* (2015), the image shown in Fig. 6(a) was convoluted with a disk-shaped mask and the resultant image is shown in Fig. 6(b). The convoluted image features local maxima, which correspond to the centers of the droplets. The locations of the droplets centers were obtained, with the corresponding results shown by the black circular data points in Fig. 6(c). The variations of the light intensity along the lines that pass through the droplets centers and are normal to the corresponding fringe pattern were considered, with a sample fringe pattern and light intensity variation for one droplet shown in Figs. 6(d) and 6(e), respectively. Then, the Fast Fourier Transform of the light intensity variation corresponding to each droplet was obtained and the number of fringes was calculated. Finally, the droplet

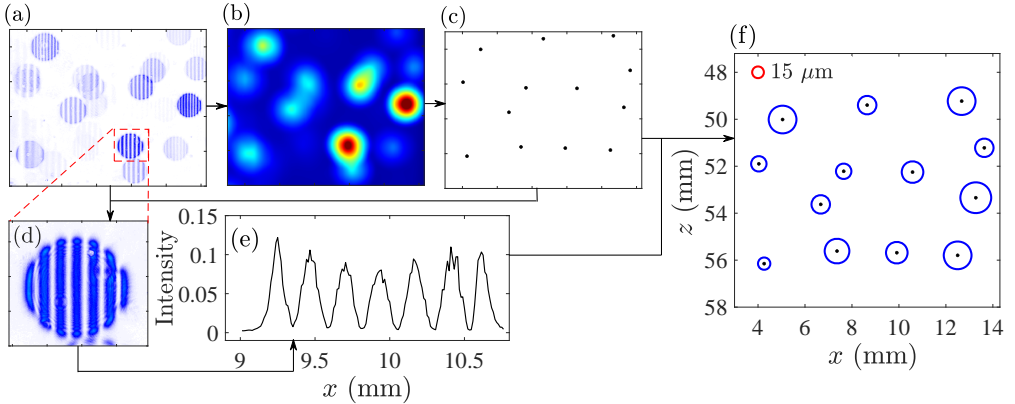


Figure 6. (a) Representative raw ILIDS image corresponding to the test condition with two perforated plates and mean bulk flow velocity of 14.0 m/s. (b) is the convolution of the results in (a) using a disk-shaped mask. (c) is the identified droplets centers. (d) is the inset of (a), highlighting a sample fringe pattern. (e) shows the variation of the light intensity normal to the fringe pattern in (d). (f) presents the droplets centers and their corresponding diameters.

diameter was calculated using the number of fringe patterns and Eq. (2.1). Figure 6(f) presents the centers of the droplets as well as the blue circles, with their diameter relating to the droplets' diameter. The diameters of the blue circles scale with the diameter of the red circle shown in the figure.

4. Results

The results are grouped into four subsections. In the first subsection, the characteristics of the background turbulent flow and the droplets diameter are discussed. In the second subsection, the degree of clustering is investigated. In the third subsection, the geometrical characteristics of the clusters and voids are presented. Finally, the joint characteristics of the clusters/voids and the droplets are presented in the last subsection.

4.1. The background flow and droplet diameter characteristics

The variations of the axial velocity mean (\bar{u}) and RMS fluctuations (u') along the x -axis are presented in the first and second rows of Fig. 7, respectively. The results in the first to fourth columns correspond to the mean bulk flow velocities of 3.5, 7.0, 10.5, and 14.0 m/s, using circular, square, triangular, and diamond-shaped data symbols, respectively. The blue, green, and red colors pertain to zero, one, and two perforated plates, respectively. The results presented in Figs. 7(a–d) feature a mean velocity deficit near $x = 0$, which is due to the wake of the spray injector, similar to the results presented in Petry *et al.* (2022). Also, the mean velocity profiles are nearly symmetric for the test conditions without a perforated plate; however, these profiles are nearly asymmetric for test conditions with one and two perforated plates, which are similar to those reported in Kheirkhah & Gülder (2015).

The results in Figs. 7(e–h) show that, for all tested mean bulk flow velocities and for the majority of the horizontal locations, the RMS of the streamwise velocity for one perforated plate is smaller than that for two perforated plates, which agrees with the results of past investigations, see for example Kheirkhah & Gülder (2015). The results in Figs. 7(e–h) also show that the values of u' for no perforated plate are larger than those of one perforated plate and close to those of two perforated plates. It is speculated that the reason for the values of u' for no perforated plate being relatively large is due to the turbulence generated

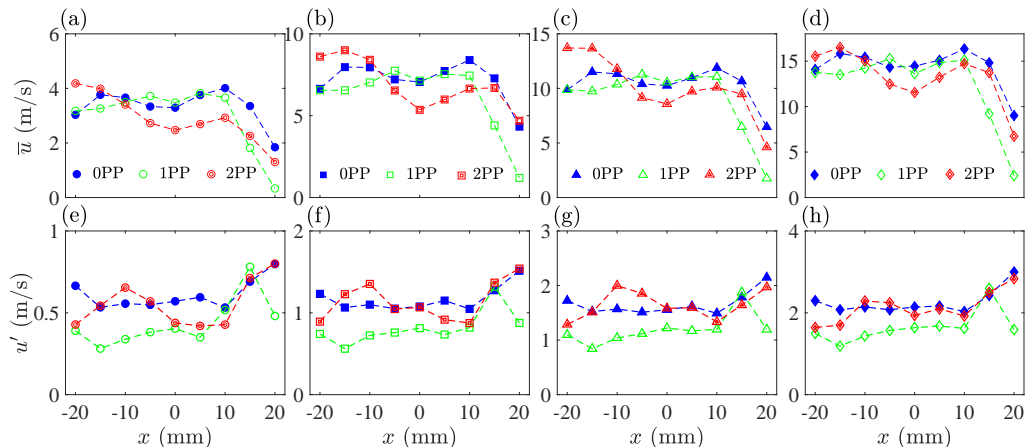


Figure 7. (a–d) are the mean streamwise velocity for the mean bulk flow velocities of 3.5, 7.0, 10.5, and 14.0 m/s, respectively. (e–h) are the root-mean-square streamwise velocity fluctuations for the mean bulk flow velocities of 3.5, 7.0, 10.5, and 14.0 m/s, respectively.

by the supporting bars of the tube-holder shown in Fig. 2(a) and the wake of the spray injector. In order to assess this speculation, HWA experiments for a free jet (without the spray injector and without the tube-holder) were performed (not presented as test conditions in Table 1), and the values of u' were obtained. These were significantly smaller than those for the first turbulence generation mechanism. For example, for $U = 7.0$ m/s and at $x = 0$, $u' = 0.34$ m/s for a free jet without the spray injector and the tube-holder; however, this parameter is 1.07 m/s with the injector and tube-holder installed (i.e. the first turbulence generation mechanism). We speculate the reason for the values of u' being relatively small for the second turbulence generation mechanism (i.e. one perforated plate) than those for the first turbulence generation mechanism (zero perforated plate) is the break up of the eddies generated in the wake of the tube-holder bars by the perforated plate. The decrease of the RMS velocity fluctuations by addition of perforated plates has been reported in for example Wang *et al.* (2019)

The PDF of the droplet diameter for the first, second, and third turbulence generation mechanisms are presented in Figs. 8(a–c), respectively. For comparison purposes, the PDF of the droplet diameter for the no co-flow test condition is overlaid on Fig. 8(a–c) using the black circular data symbol. For the probability density function calculations, an $11.5 \mu\text{m}$ droplet diameter bin size was used, since this led to the best presentation of the results. For all test conditions, the mean (\bar{d}) and most probable (d^*) droplet diameters were obtained and presented in Figs. 9(a) and (b), respectively. In these figures, the error bars present twice the RMS of the droplet diameter fluctuations. The results presented in Fig. 8 show that the presence of the co-flow and increasing the mean bulk flow velocity do not significantly change the PDF of the droplet diameter. Also, comparison of the results presented in Fig. 8 suggests that changing the turbulence generation mechanism does not change the PDF of the droplet diameter noticeably. Although the droplets diameter PDF estimated in the entire domain of investigation is not sensitive to the tested mean bulk flow velocity and the utilized turbulence generation mechanism, it is yet to be investigated how/if these parameters influence the PDF of the droplet diameter within the clusters and voids, which are studied in the following subsections.

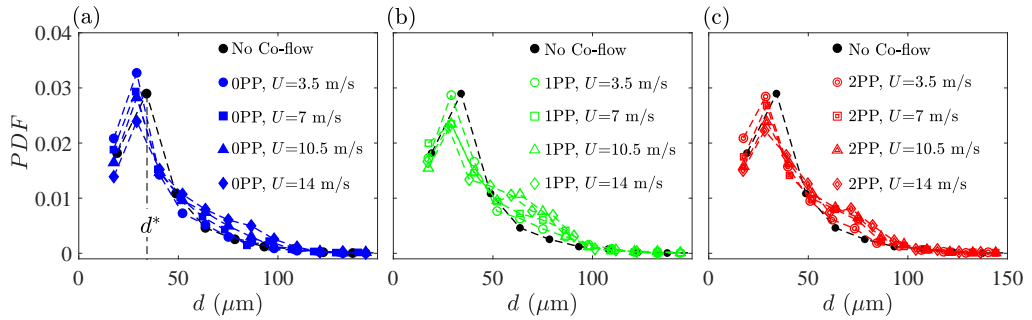


Figure 8. (a–c) are the probability density functions of the droplet diameter for no perforated plate, one perforated plate, and two perforated plates, respectively. The black circular data points are the PDF of the no co-flow test condition and is repeating in (a–c) for comparison purposes.

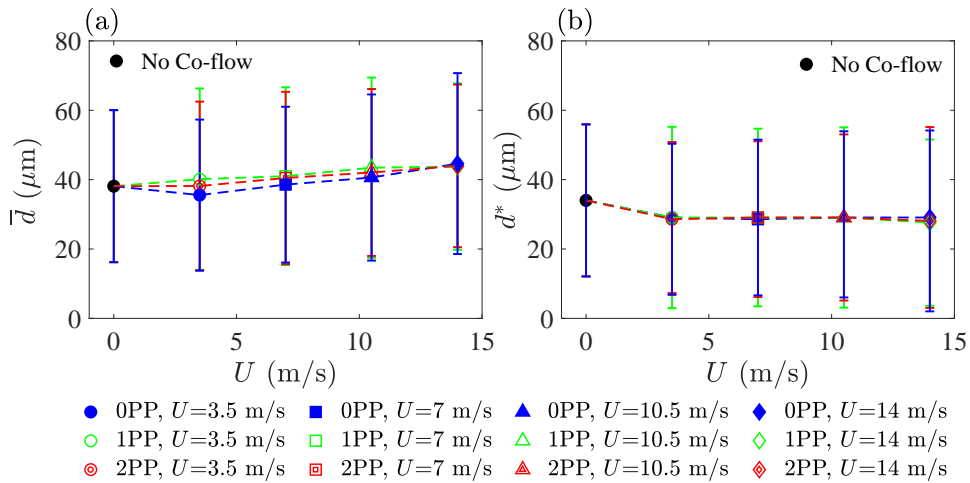


Figure 9. (a) and (b) are the variations of the mean and most probable droplet diameter versus the mean bulk flow velocity for all test conditions.

4.2. The droplets degree of clustering

The Voronoi cells were used to study the droplets degree of clustering, following the procedure discussed in subsection 3. For all test conditions, the PDFs of the Voronoi cells area (A) are calculated and presented in Fig. 10(a). Also, the PDFs of the Voronoi cells area normalized by the mean area (A/\bar{A}) are presented in Fig. 10(b) for all test conditions. As can be seen, the PDFs of A/\bar{A} collapse for all tested conditions, which is similar to the results presented in Obligado *et al.* (2014) and Monchaux *et al.* (2010). Overlaid on Fig. 10 is the PDF of the normalized area of the Voronoi cells provided these cells are spatially distributed following the Random Poisson Process, with the formulation of PDF_{RPP} presented in Eq. (3.1). The results in Fig. 10 show that, for all test conditions, the PDFs of A/\bar{A} intersect with PDF_{RPP} at $A/\bar{A} = 0.5$ and 2.2 , which are shown by the vertical dashed lines in Fig. 10(b) and are similar to those shown in Fig. 5(c). Using the above normalized areas and following the procedure presented in subsection 3.1, the clusters and voids were identified, and their degree of clustering is studied below.

The degree of clustering, $(\sigma - \sigma_{RPP})/\sigma_{RPP}$, is presented in Fig. 11(a) for all test conditions.

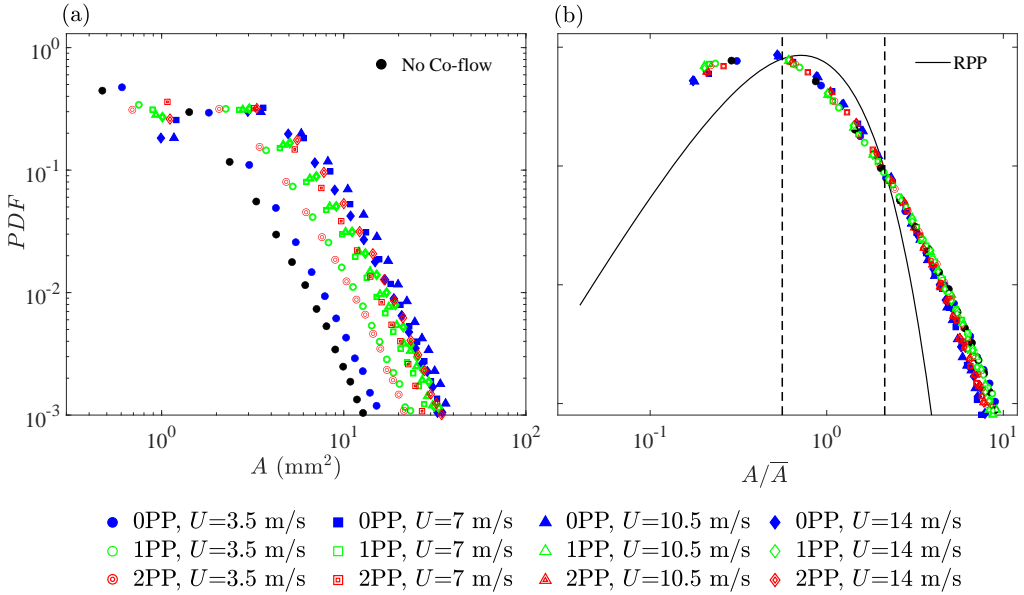


Figure 10. (a) The probability density functions of the Voronoi cells area, $PDF(A)$, for all test conditions. (b) is the PDF of Voronoi cells area normalized by the mean area. The solid black curve in (b) is the PDF of the normalized Voronoi cells area provided they were distributed following a Random Poisson Process, with the formulation given in Eq. (3.1). The dashed lines in (b) correspond to $A/\bar{A} = 0.5$ and 2.2 .

The results in the figure show that, for the mean bulk flow velocities larger than or equal to 3.5 m/s, the presence of the turbulent co-flow increases the degree of clustering for one perforated plate (compared to no co-flow); however, for test conditions with zero and two perforated plates, the presence of the co-flow generally decreases the degree of clustering. For comparison purposes, the variation of the degree of clustering versus the Stokes number is presented in Fig. 11(b). In addition to the results of the present study, those of Obligado *et al.* (2014); Monchaux *et al.* (2010); Sumbekova *et al.* (2017); Petersen *et al.* (2019) are also overlaid on the figure. The results show that increasing the Stokes number from 0 to about 10 increases the degree of clustering from about 0 to 1.2; however, this parameter nearly plateaus at around 0.7 to 1 for $St \gtrsim 5$. Wang *et al.* (2020) performed 3D Direct Numerical Simulation (DNS) of particles clustering in homogeneous and isotropic turbulent flow in a box for Stokes numbers ranging from about 0 to 7. They estimated the standard deviation of the 3D Voronoi cells volume. Results of Wang *et al.* (2020) show that the standard deviation of the 3D Voronoi cells volume increases by increasing the Stokes number from about 0 to 1. However, further increase of the Stokes number to about 7 plateaus the standard deviation of the Voronoi cells volume. Acknowledging that the analysis of Wang *et al.* (2020) is performed for the RMS of the Voronoi cells volume (which is different from the degree of clustering that pertains to the Voronoi cells area), the reported trend in Wang *et al.* (2020) follows that presented in Fig. 11(b) for matching Stokes numbers. Nevertheless, to our best knowledge, the plateau of the degree of clustering with increasing the Stokes number for $St \gtrsim 7$ is reported in the present study for the first time.

4.3. The geometrical characteristics of clusters and voids

The spatial distribution and length scale of the clusters and voids as well as how these are influenced by the non-dimensional parameters are discussed in the following subsections.

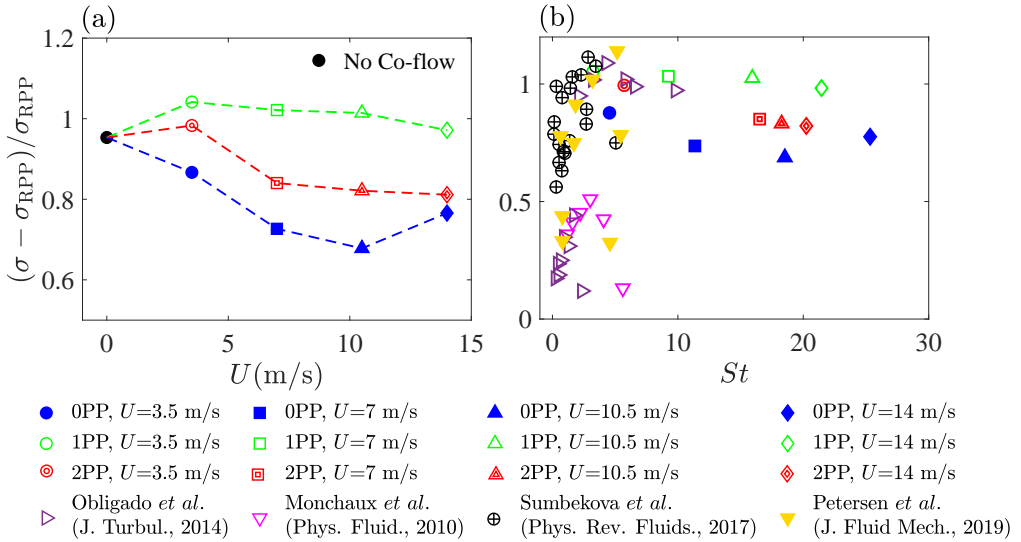


Figure 11. (a) and (b) are the degree of clustering versus the mean bulk flow velocity and the Stokes number, respectively. Overlaid on (b) are the results of Obligado *et al.* (2014); Monchaux *et al.* (2010); Sumbekova *et al.* (2017); Petersen *et al.* (2019).

4.3.1. Characteristics of clusters and voids spatial distribution

Although the analysis presented in subsection 4.2 allows for understanding the droplets degree of clustering, it does not provide insight into the characteristics of the clusters and voids themselves. In this subsection, it is of interest to investigate if the clustering of the clusters and voids occurs, how the clusters and voids are spatially distributed, what the length scale of clusters and voids are, and how/if the non-dimensional parameters influence the above.

A representative spatial distribution of the clusters for the no co-flow test condition is presented in Fig. 12(a), see the blue regions in the figure. The centers of the area of the clusters were obtained and are shown by the black circular symbols in both Figs. 12(a and b). The Voronoi cells associated with the center of areas of the clusters were obtained and are shown in Fig. 12(b) using the blue lines. For all test conditions, the Probability Density Function of the Voronoi cells area obtained using the center area of the clusters (\bar{A}) divided by its mean value ($\bar{\bar{A}}$) is presented in Fig. 13. Also overlaid on the figure is the PDF_{RPP} . As can be seen, the PDFs of $\bar{A}/\bar{\bar{A}}$ for all test conditions nearly collapse on PDF_{RPP} , suggesting that the centers of area of the clusters are distributed following a Random Poisson Process. Thus, the clustering of the clusters does not occur for the conditions tested in the present study. A similar analysis was performed to understand if the clustering of the voids occurs. Since the voids are positioned at the periphery of the domain of investigation, see for example Fig. 5(f), the vertices of the Voronoi cells generated from the voids center of area cannot be accessed. Thus, for the spray and co-flow configuration of the present study, the clustering of the voids cannot be investigated.

The spatial probabilities of finding clusters and voids were calculated using their geometrical locations, such as those shown in Fig. 5(e and f). For clusters, the blue regions, for example those in Fig. 5(e), were assigned a unity value and the rest of the domain of investigation was assigned zero. Then, all binarized results were averaged and was referred to as the spatial probability of finding clusters. A similar procedure was followed to obtain the

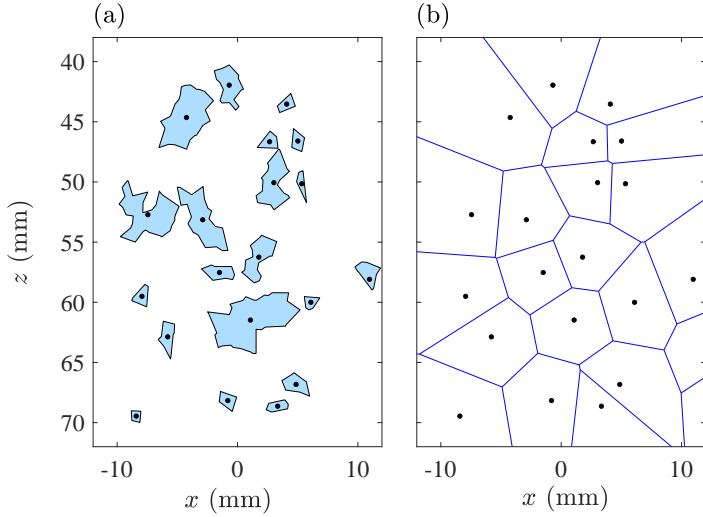


Figure 12. (a) Representative clusters. (b) The Voronoi cells formed by the clusters center of area. In both (a) and (b), the clusters center of area are shown by the solid black data symbol. The results in (a) and (b) correspond to the no co-flow test condition.

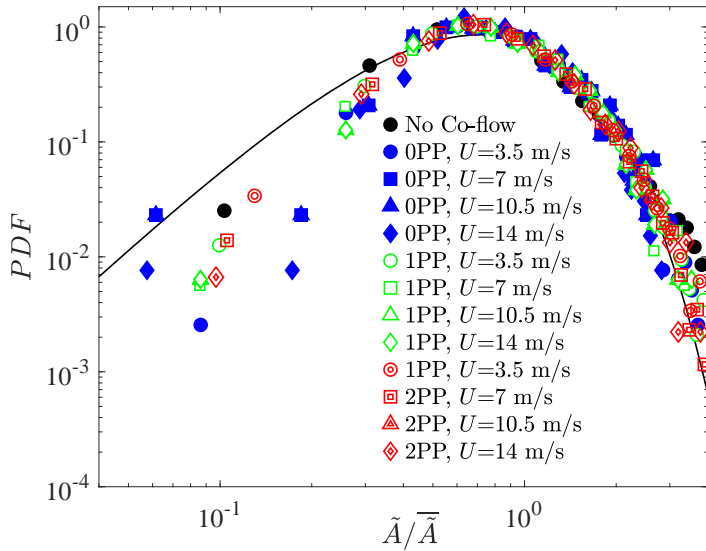


Figure 13. The probability density functions of the normalized Voronoi cells area formed by the clusters center of area. The black solid curve is the PDF_{RPP} .

probability of finding voids in the domain of investigation using the location of voids such as that shown in Fig. 5(f). The spatial probabilities of finding clusters and voids were overlaid together and presented in Fig. 14 using the blue and green color contours, respectively. In Fig. 14, the first column presents the results for the no co-flow test condition, is repeating, and is presented for comparison purposes. The second to fifth columns correspond to the mean bulk flow velocities of 3.5, 7.0, 10.5, and 14.0 m/s, respectively. The results in Figs. 14(b–e), (g–j), and (l–o) correspond to test conditions with zero, one, and two perforated plates,

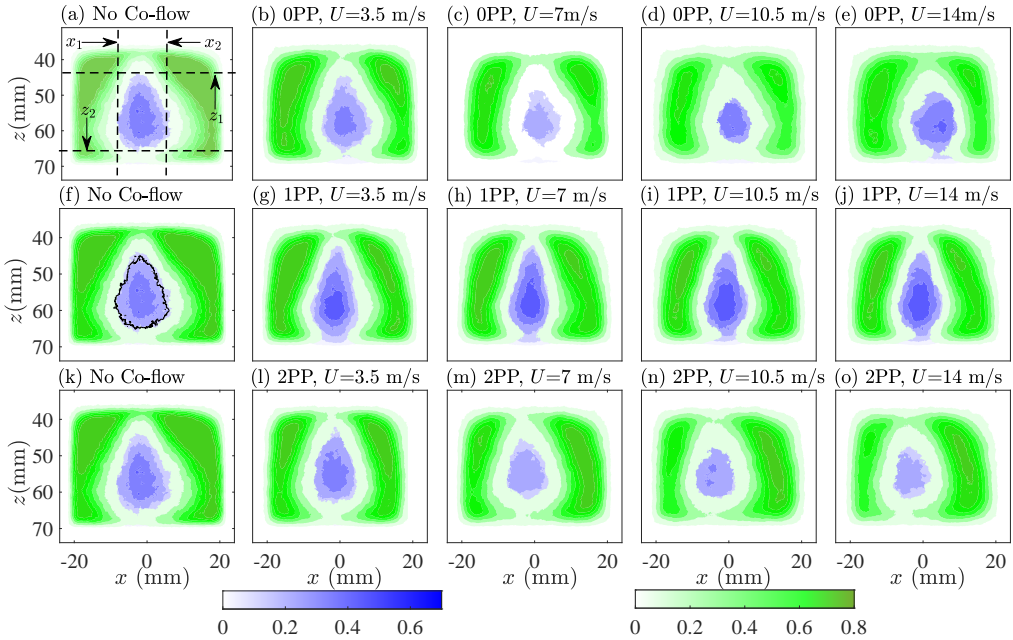


Figure 14. The blue and green contours present the probabilities of finding clusters and voids, respectively. The first to fifth columns correspond to no co-flow, $U = 3.5, 7.0, 10.5,$ and 14.0 m/s, respectively. The results in (b–e), (g–j), and (l–o) pertain to the first to third turbulence generation mechanisms, respectively.

respectively. As can be seen, the probability of finding clusters is maximized at the spray core, which is similar to the findings of Zimmer *et al.* (2003) and Jedelsky *et al.* (2018). Compared to the clusters, the probability of finding voids is maximized at the periphery of the domain of investigation. It can also be seen that the shape of the region with a relatively large probability of finding the clusters change by changing the test condition. In order to quantify this, the contour that corresponds to 20% probability of finding the clusters was obtained for all test condition, with that for the no co-flow test condition overlaid by the black solid curve in Fig. 14(f). Sample boundaries of such contours for the no co-flow test condition are shown by $x_1, x_2, z_1,$ and z_2 in Fig. 14(a). The horizontal ($x_2 - x_1$) and vertical ($z_2 - z_1$) extents of the above boundaries were obtained for all test conditions, with the results shown in Fig. 15(a) and (b), respectively. As can be seen in Fig. 15(b), the presence of the co-flow (compared to the no co-flow test condition) decreases the horizontal extents of the regions with a large probability (more than 20%) of finding clusters. A similar observation is made for the vertical extent of these regions for the first and third turbulence generation mechanisms. However, the presence of the co-flow elongates the above regions vertically for the second turbulence generation mechanism.

In order to study the reason for the above observations, $z_2 - z_1$ versus Re_λ and St are presented in Figs. 16(a) and (b), respectively. Also, variations of $x_2 - x_1$ versus Re_λ and St are presented in Figs. 16(c) and (d), respectively. Comparison of the results in Fig. 16(a and b) with those in Fig. 16(c and d) suggests, although $z_2 - z_1$ is significantly influenced by Re_λ and St , $x_2 - x_1$ does not change remarkably with these non-dimensional parameters. For a fixed value of Re_λ , see the dashed line in Fig. 16(a), increasing the Stokes number, see the corresponding dashed arrow in Fig. 16(b), increases $z_2 - z_1$. However, for a fixed value of the Stokes number, see the solid line in Fig. 16(b), increasing the Reynolds number decreases $z_2 - z_1$, see the solid arrow in Fig. 16(a). This means that, for test conditions that feature

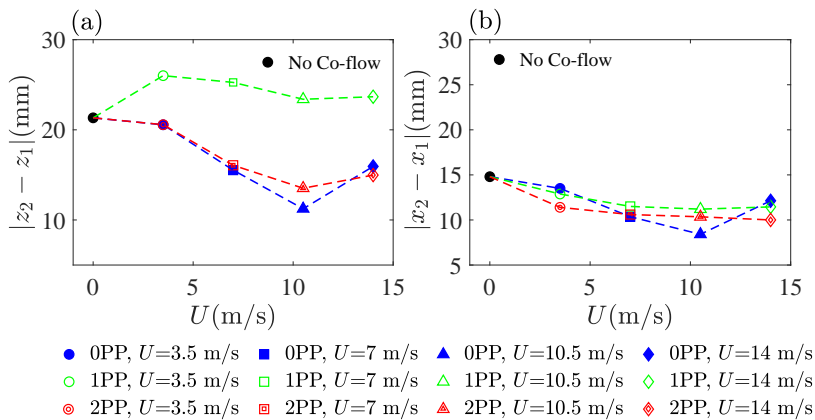


Figure 15. (a) and (b) are the variations of the vertical and horizontal extents of the regions that feature more than 20% probability of finding clusters versus the mean bulk flow velocity, respectively.

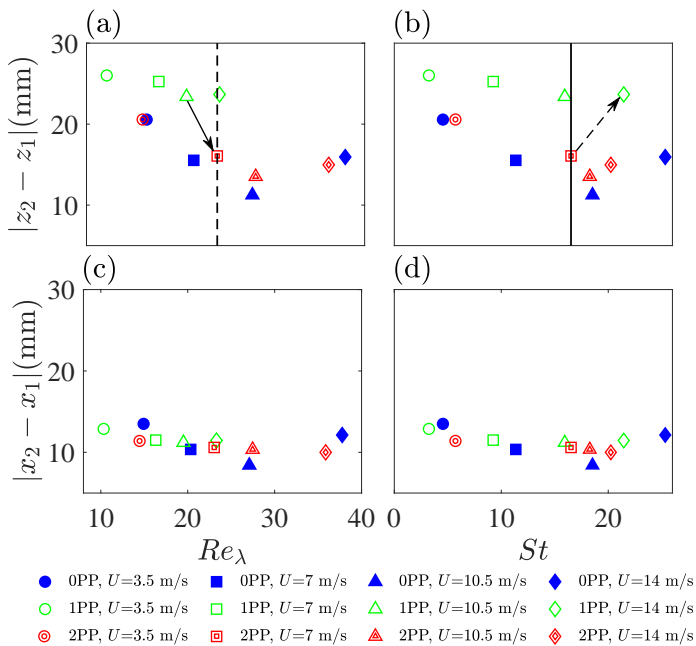


Figure 16. (a) and (b) are the vertical extent of the regions that feature more than 20% probability of finding clusters versus Re_λ and St , respectively. (c) and (d) are the horizontal extent of the regions that feature more than 20% probability of finding clusters versus Re_λ and St , respectively.

similar background Re_λ , increasing the inertia of the droplets increases the probability of finding clusters at a relatively large range of vertical distances from the injector. Although, for a fixed Reynolds number, it is anticipated that increasing the Stokes number should increase the probability of finding droplets at large distances from the injector, the results in Fig. 16(b) suggest that the droplets continue to cluster at large distances from the injector.

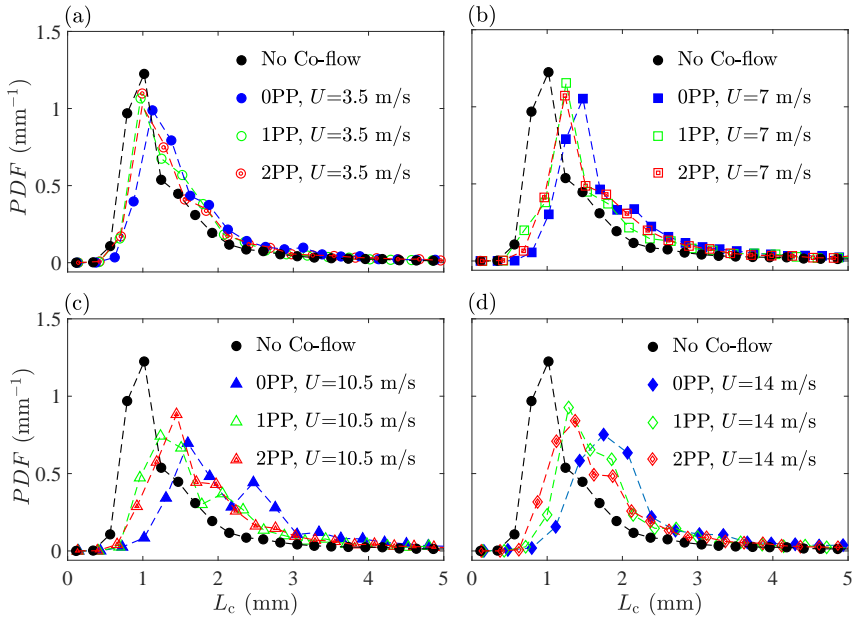


Figure 17. (a–d) are the PDFs of the cluster length scale for mean bulk flow velocities of $U = 3.5, 7.0, 10.5,$ and 14.0 m/s, respectively. Overlaid by the black circular data symbol in (a–d) is the PDF of the cluster length scale for the no co-flow test condition.

4.3.2. Length scale of clusters and voids

Following Petersen *et al.* (2019), the cluster and void length scales were defined as $L_c = \sqrt{A_c}$ and $L_v = \sqrt{A_v}$, respectively, with A_c and A_v being the cluster and void areas. The PDFs of L_c and L_v are presented in Figs. 17 and 18, respectively. The results in Figs. 17(a–d) and 18(a–d) correspond to mean bulk flow velocities of 3.5, 7.0, 10.5, and 14.0 m/s, respectively. For comparison purposes, the PDFs of the cluster and void length scales corresponding to the no co-flow condition is presented by the solid black circular data symbol on the figures. The results in Fig. 17 show that, for a given turbulence generation mechanism, the most probable cluster and void length scales increase by increasing the mean bulk flow velocity. It is also observed that, for a given mean bulk flow velocity, the most probable cluster and void length scales are largest for the test conditions with no perforated plates. Compared to the effects of U and turbulence generation mechanism on the most probable cluster length scale, the most probable void length scale does not change by changing the above parameters.

Although the above analysis related to the most probable cluster and void length scales are of importance, majority of past investigations studied the relations between the mean values of the above length scales and the non-dimensional parameters, such as Taylor length scale based-Reynolds and Stokes numbers. The mean cluster and void length scales versus the mean bulk flow velocity are presented in Figs. 19(a) and (b), respectively. The error bars in the figures are twice the standard deviation of the corresponding data. For comparison purposes, the Taylor and integral length scales are also presented in Figs. 19(c) and (d), respectively. As can be seen, increasing the mean bulk flow velocity slightly increases the mean cluster size, however, the mean void size remains nearly constant. The results show that cluster size is larger than the Taylor length scale but smaller than the integral length scale. The mean void length scale is, however, close to the integral length scale.

Variations of $\overline{L_c}$ normalized by the Kolmogorov length scale versus Re_λ is presented in

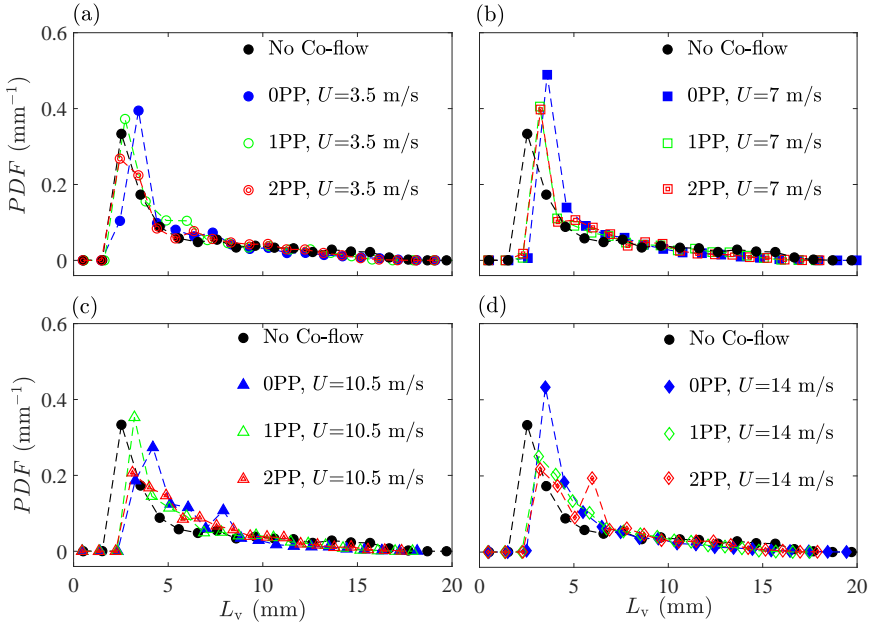


Figure 18. (a–d) are the PDFs of the void length scale for the mean bulk flow velocities of 3.5, 7.0, 10.5, and 14.0 m/s, respectively. The black circular data symbol is the PDF of the void length scale for the no co-flow test condition.

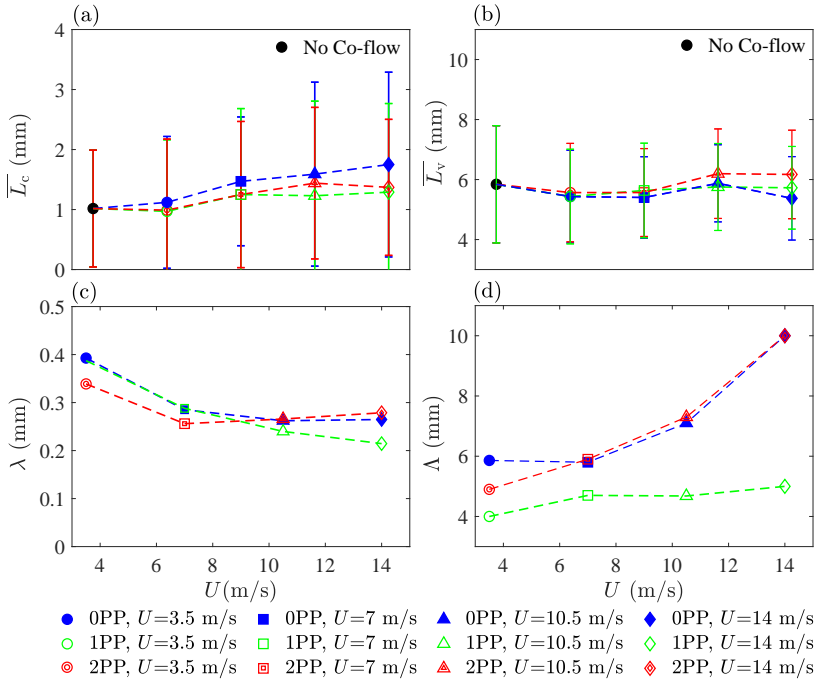


Figure 19. (a) and (b) are the mean cluster and void length scales versus the mean bulk flow velocity, respectively. (c) and (d) are the Taylor and integral length scales versus the mean bulk flow velocity, respectively.

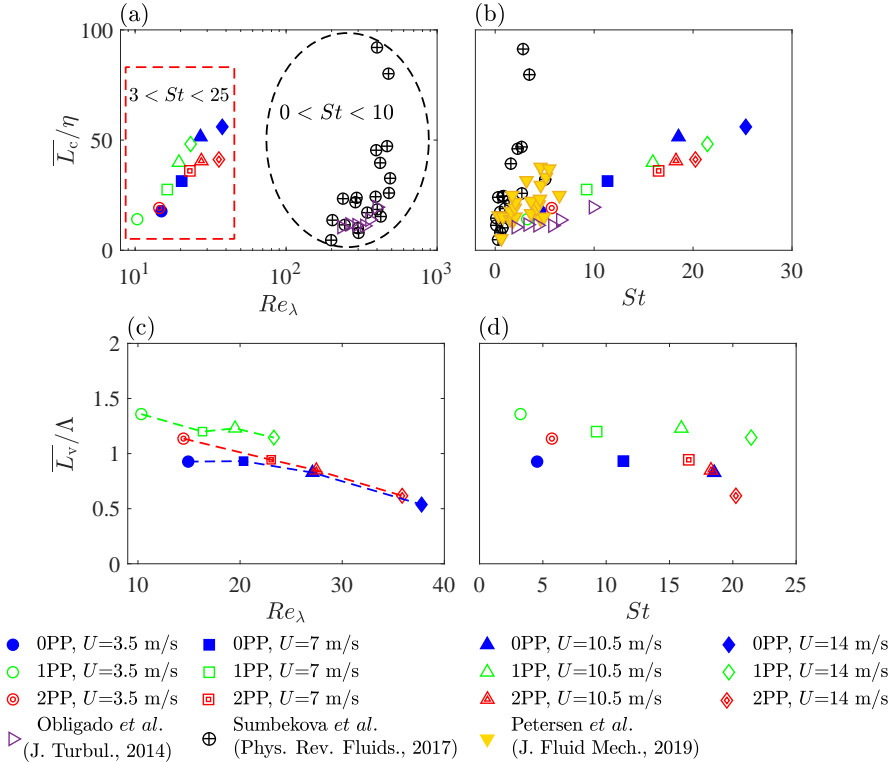


Figure 20. (a) and (b) are the mean cluster length scale normalized by the Kolmogorov length scale versus Re_λ . Overlaid on (a and b) are the results of Obligado *et al.* (2014), Sumbekova *et al.* (2017), and Petersen *et al.* (2019). (c) and (d) are the mean void length scale normalized by the integral length scale versus Re_λ and St , respectively.

Fig. 20(a). Also, overlaid on the figure are the results of Obligado *et al.* (2014) and Sumbekova *et al.* (2017), which are highlighted by the black dashed ellipse in the figure and correspond to relatively small Stokes numbers ($0 \lesssim St \lesssim 10$). The results of the present study are highlighted by the dashed red rectangle. As can be seen, the normalized cluster length scale of the present study and those of Obligado *et al.* (2014) and Sumbekova *et al.* (2017) do not follow a trend. Thus, variation of $\overline{L_c}/\eta$ versus the Stokes number were obtained and presented in Fig. 20(b). The results of Obligado *et al.* (2014); Sumbekova *et al.* (2017) as well as Petersen *et al.* (2019) are overlaid on the figure for comparison. As can be seen, the normalized mean cluster length scale follows a trend when presented against the Stokes number. Specifically, it can be seen that increasing St almost linearly increases $\overline{L_c}/\eta$. Variations of $\overline{L_v}/\Lambda$ versus Re_λ and St are presented in Fig. 20(c) and (d), respectively. Compared to the mean cluster length scale that can become about 100 times larger than the Kolmogorov length scale, the results in Fig. 20(c and d) show that the mean void length scale is on the order of the integral length scale. For large Stokes numbers, the droplets feature relatively large inertia, they interact with large scale eddies, and as a result, the droplets position at the periphery of the large scale eddies. This would suggest that, for large Stokes numbers (such as those of the present study), the regions inside the large eddies correspond to voids; and, as a result, these regions size is about the voids length scale, as shown in Fig. 20(d). Yoshimoto & Goto (2007) performed DNS of particles interacting with homogeneous and isotropic turbulence in a box, and they, indeed, showed that for $St = 10$, the length scale of voids saturate at the integral length scale

of the turbulent flow. The results of the present study extends the DNS of Yoshimoto & Goto (2007) from homogeneous and isotropic turbulence in a box to sprays in a turbulent co-flow with Stokes numbers up to 25.

4.4. *The inter-cluster and inter-void characteristics*

The results discussed in subsections 4.1–4.3 allow for understanding the characteristics of the droplets as well as those of clusters and voids individually; however, our understanding related to joint characteristics of the droplets and clusters/voids remains to be developed. In the following, the number density of the droplets inside the clusters and voids as well as the Joint Probability Density Function (JPDF) of the droplets diameter and clusters/voids areas are investigated.

4.4.1. *Number densities of droplets inside clusters and voids*

Figure 21 presents the JPDF of the number of droplets (N_P) inside the clusters and the area of the clusters. The contours are presented in a logarithmic scale (with a base of 10) for improving the clarity of presentation. The JPDFs in the first column correspond to the no co-flow test condition, are repeating, and are presented for comparison purposes. The results in the second to fifth columns pertain to the mean bulk flow velocities of 3.5, 7.0, 10.5, and 14.0 m/s, respectively. The results in (b–e), (g–j), and (l–o) correspond to zero, one, and two perforated plates, respectively. As can be seen, there exists a positive correlation between the number of particles and the area of the clusters, i.e. larger clusters contain more droplets. It can also be seen that increasing the mean bulk flow velocity decreases the slope of the relation between N_P and A_c , suggesting that the clusters dilute with increasing U . In order to quantify this, the combination of (N_P , A_c) data points at which the JPDF significantly changes by changing A_c at a fixed N_P were obtained, with representative results shown by the white circular data symbols in Fig. 21(a). The linear fits to these white data points were obtained, and the slopes of the lines were referred to as m_1 and m_2 . Variations of m_1 , m_2 , and their average, $\bar{m} = 0.5(m_1 + m_2)$, versus the mean bulk flow velocity are shown in Figs. 22(a–c), respectively. These parameters quantify the number density of the droplets within the clusters. Similar to the above analysis, the JPDF of the number of droplets inside the voids and the area of the voids were obtained, with the corresponding results presented in Fig. 23. The figure indicators in Fig. 23 are identical to those in Fig. 21. Similar to the analysis presented for the results in Fig. 21(a–c), the slopes (m'_1 , m'_2 , and $\bar{m}' = 0.5(m'_1 + m'_2)$) for the results in Fig. 23 were extracted and are shown in Fig. 22(d–f). Comparison of the results presented in Fig. 22(a–c) with those in Fig. 22(d–f) suggests that the number density of droplets within the clusters are generally one order of magnitude larger than that in the voids.

To investigate the effect of the non-dimensional parameters on the above number densities, the variations of \bar{m} versus the Reynolds and Stokes numbers are presented in Figs. 24(a) and (b), respectively. Also overlaid on the figures are the error bars, whose lengths correspond to $m_2 - m_1$. Similarly, the variations of \bar{m}' versus the Reynolds and Stokes numbers are also shown in Figs. 24(c) and (d), respectively, with the lengths of the error bars being $m'_2 - m'_1$. The results suggest that, for $St \gtrsim 10$, the number densities of the droplets inside the clusters and voids are nearly independent of the Stokes and Reynolds numbers and equal 0.67 and 0.05 mm^{-2} , respectively. However, for $St \lesssim 10$, increasing the Reynolds number (which is accompanied by increase of the Stokes number) nearly decreases the number densities of the droplets in the clusters and voids.

On one hand, the results presented in Fig. 4 showed that increasing the Reynolds and Stokes numbers both decrease the spray volume fraction. On the other hand, for $St \lesssim 10$, the results in Fig. 24 showed that increasing both Re_λ and St also decrease \bar{m} and \bar{m}' . It is of

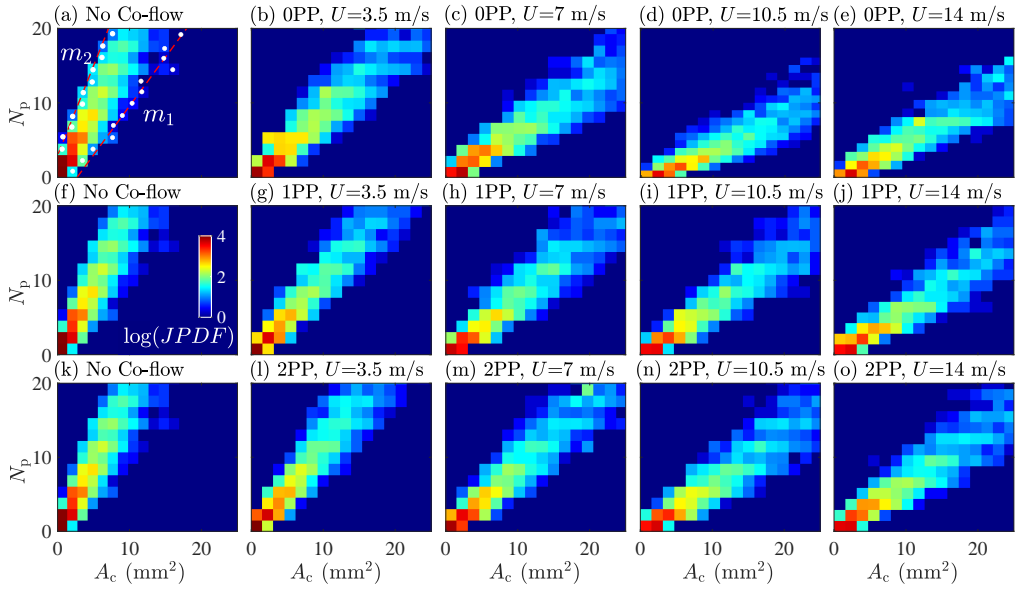


Figure 21. The logarithmic joint probability density function of the number of droplets within a given cluster area. The first column corresponds to the no co-flow test condition and is repeating in each row for comparison purposes. The second to fifth columns correspond to the mean bulk flow velocities of 3.5, 7.0, 10.5, and 14.0 m/s, respectively. (b–e), (g–j), and (l–o) pertain to the first to third turbulence generation mechanisms, respectively.

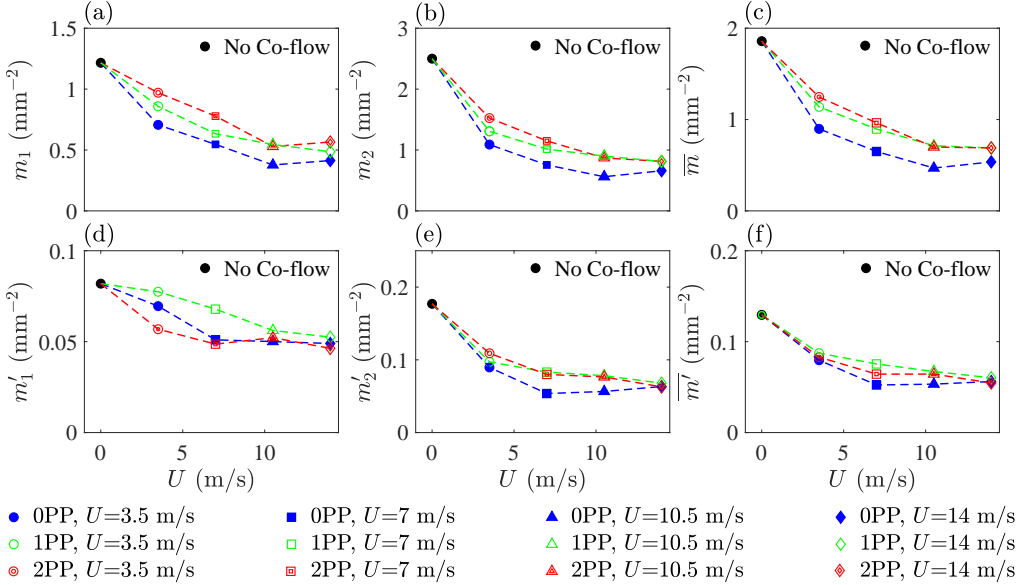


Figure 22. (a–c) are variations of m_1 , m_2 , and $0.5(m_1 + m_2)$ versus U , respectively. (d–f) are variations of m'_1 , m'_2 , and $0.5(m'_1 + m'_2)$ versus U , respectively.

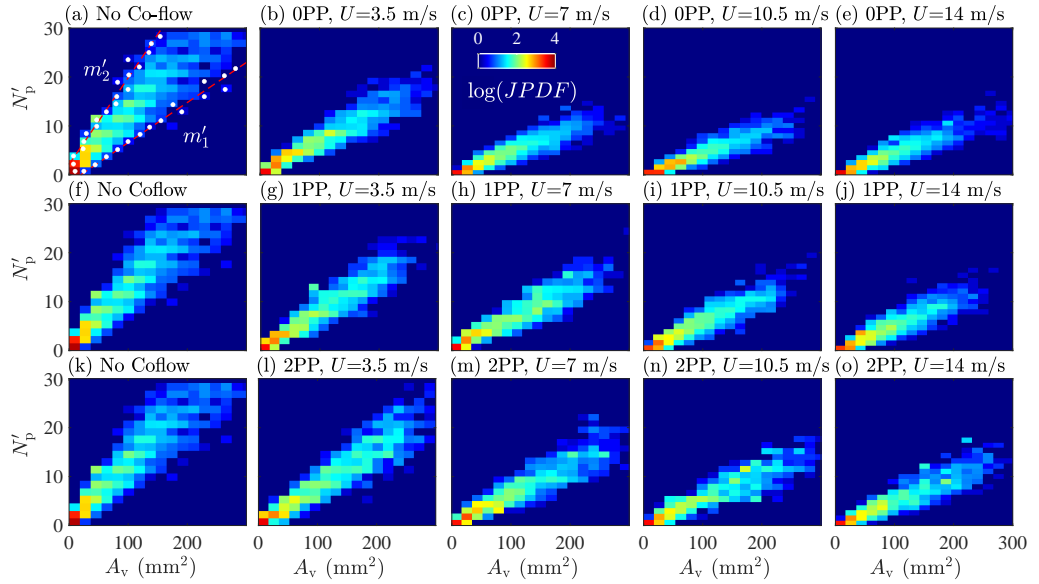


Figure 23. The logarithmic joint probability density function of the number of droplets and void area. The first column corresponds to the no co-flow test condition and is repeating in each row for comparison purposes. The second to fifth columns correspond to the mean bulk flow velocities of 3.5, 7.0, 10.5, and 14.0 m/s, respectively. (b–e), (g–j), and (l–o) pertain to the first to third turbulence generation mechanisms, respectively.

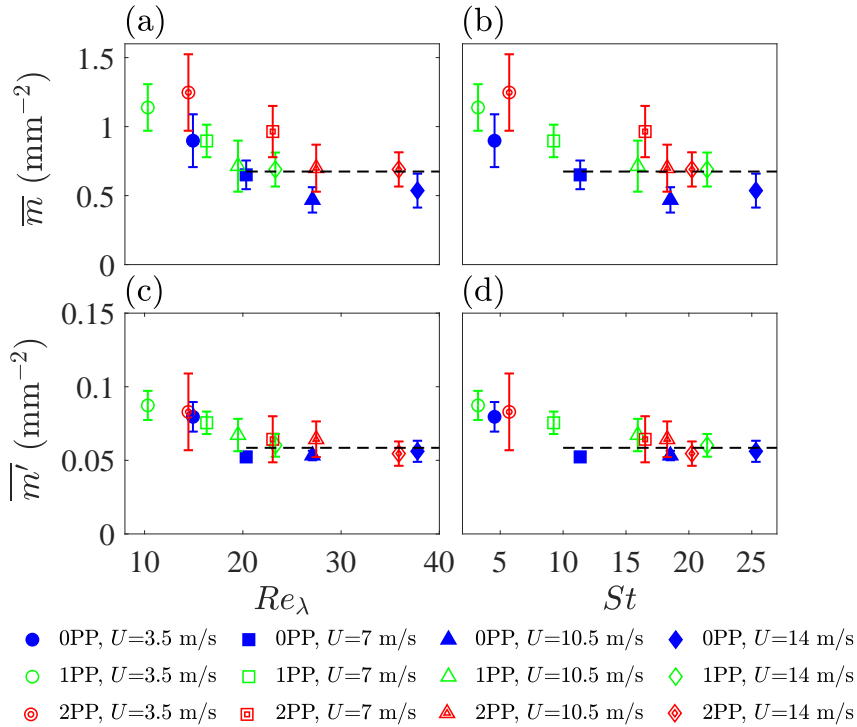


Figure 24. (a) and (b) are variations of \bar{m} versus Re_λ and St , respectively. (c) and (d) are variations of \bar{m}' versus Re_λ and St , respectively.

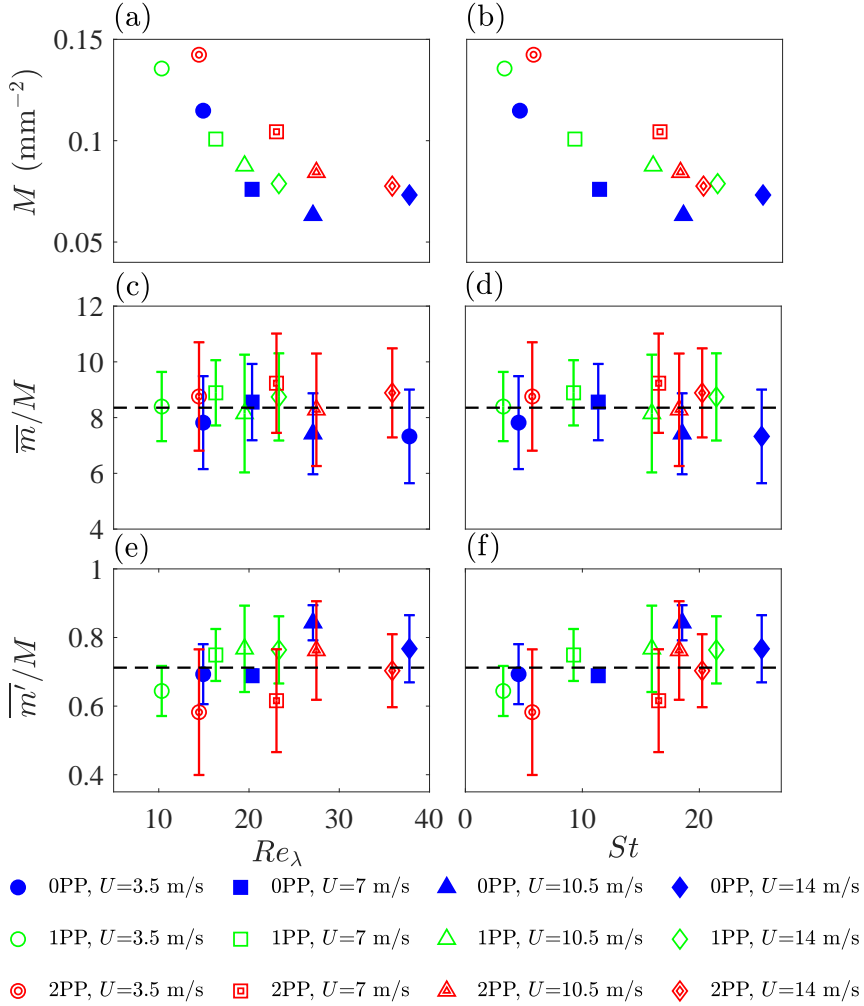


Figure 25. (a) and (b) are the variations of the total number density versus Re_λ and St , respectively. (c) and (d) are the variations of the number density of droplets in the clusters divided by the total number density versus Re_λ and St , respectively. (e) and (f) are the variations of the number density of droplets in the voids divided by the total number density versus Re_λ and St , respectively.

interest to investigate the contributions of the decay of the number densities of the droplets inside the clusters and voids to the potential decay in the total number density of the droplets and if these contributions change by changing Re_λ and St . Figure 25(a) and (b) present the ratio of the total number of droplets detected in the Mie scattering field of view divided by the area of the field of view, M , versus the Reynolds and Stokes numbers, respectively. As can be seen, increasing these non-dimensional parameters decrease M , which is anticipated considering the decreasing trend in Fig. 4(c) and that the most probable droplet diameter is nearly unchanged by changing the test conditions. The variations of \bar{m}/M versus Re_λ and St are presented in Figs. 25(c) and (d). Similarly, the variations of \bar{m}'/M versus Re_λ and St are presented in Figs. 25(e) and (f), respectively. In Figs. 25(c and d) and (e and f), the lengths of the error bars are $m_2 - m_1$ and $m'_2 - m'_1$ normalized by the total droplets number density of the corresponding test condition. The results show that the number density of the droplets

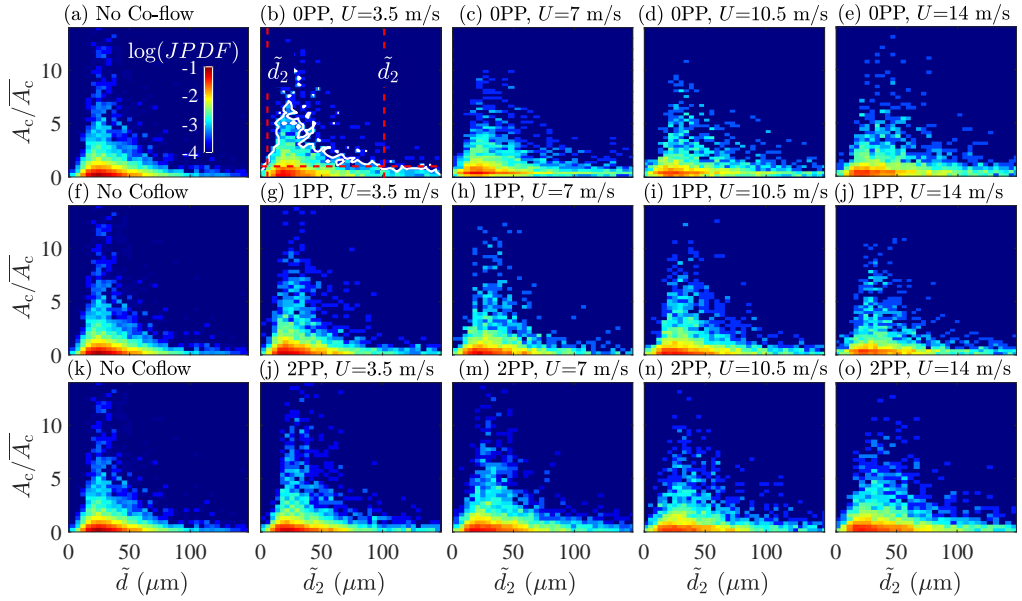


Figure 26. The logarithmic joint probability density function of the normalized clusters area ($A_c/\overline{A_c}$) and the mean diameter (\tilde{d}) of the droplets that exist within the cluster with normalized area of $A_c/\overline{A_c}$. The first column corresponds to the no co-flow test condition and is repeating in each row for comparison purposes. The second to fifth columns correspond to the mean bulk flow velocities of 3.5, 7.0, 10.5, and 14.0 m/s, respectively. (b–e), (g–j), and (l–o) present the results for the first to third turbulence generation mechanisms, respectively.

within the clusters and voids are 8.3 and 0.7 times the total number density, see the dashed lines in the figures, and these ratios do not change by changing the test conditions.

4.4.2. Joint probability density function of droplet diameter and cluster/void area

The joint probability density function of the clusters normalized area ($A_c/\overline{A_c}$) and the mean diameter (\tilde{d}) of the droplets within the clusters with normalized area of $A_c/\overline{A_c}$ is presented in Fig. 26. For presentation purposes, the JPDF contours are shown in a logarithmic scale with the base of 10. The results presented in the first column pertain to the no co-flow test condition, are identical, and are shown for comparison purposes. The contours presented in the second to fifth columns correspond to the mean bulk flow velocities of 3.5, 7.0, 10.5, and 14.0 m/s, respectively. The results in Figs. 26(b–e), (g–j), and (l–o) pertain to test conditions with zero, one, and two perforated plates, respectively. As can be seen, for all test conditions, the clusters with relatively small areas ($A_c/\overline{A_c} \lesssim 1$) are highly likely to exist. This is due to the PDF of the cluster length scale being skewed towards small values, as shown in Fig. 17. It can also be seen that near $\tilde{d} \approx 30 \mu\text{m}$, which is close to the most probable droplet diameter measured in the ILIDS field of view and tabulated in Table 1, the JPDFs feature significant values for a large range of cluster sizes. This means that, for all test conditions, the majority of the clusters carry the droplets with the most probable diameter.

Comparison of the JPDFs for the no co-flow test condition (see the first column) with those that the co-flow was provided shows that the probability of finding large droplets (mean diameter larger than about $100 \mu\text{m}$) within a given normalized cluster area increases by adding the co-flow. This means that the presence of the co-flow facilitates the clustering of the large droplets. In order to quantify the effect of the co-flow on \tilde{d} , the contour of

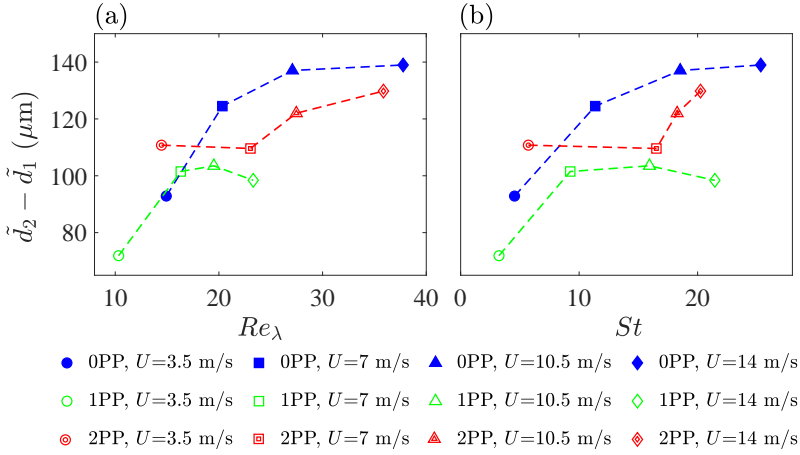


Figure 27. (a) and (b) are the variations of $\tilde{d}_2 - \tilde{d}_1$ versus the Reynolds and Stokes numbers, respectively.

$JPDF(A_c/\overline{A_c}) = 10^{-3.5}$ was considered. Then, the intersections of this contour with a given normalized cluster area (here, $A_c/\overline{A_c} = 1$) were obtained, which are referred to as \tilde{d}_1 and \tilde{d}_2 , see Fig. 26(b). The values of \tilde{d}_1 and \tilde{d}_2 change by varying the values of the selected $JPDF$ as well as the selected $A_c/\overline{A_c}$; however, the trends of variation for $\tilde{d}_2 - \tilde{d}_1$ with the governing parameters are independent of the selected $JPDF$ value and $A_c/\overline{A_c}$. For all test conditions with the co-flow, the variations of $\tilde{d}_2 - \tilde{d}_1$ versus Re_λ and St were obtained and presented in Fig. 27(a) and (b), respectively. The results show that increasing Re_λ and St generally increases $\tilde{d}_2 - \tilde{d}_1$. As shown in Fig. 19(d) and as tabulated in Table 1, increasing the mean bulk flow velocity increases the integral length scale and decreases the Kolmogorov length scale. Thus, adding the co-flow (which is equivalent to increasing the Re_λ) increases the range of the turbulent eddy sizes. Following the mechanisms proposed in for example Goto & Vassilicos (2006), since turbulent eddies are responsible for the clustering of the droplets, the larger range of turbulent eddy sizes (see Figs. 19(c and d)) could increase the possibility of a broader range of droplet diameters to be positioned inside the clusters. As a result, a positive relation between $\tilde{d}_2 - \tilde{d}_1$ and Re_λ as well as St is observed. This also suggests that the mechanism proposed in for example Goto & Vassilicos (2006) for droplets clustering may be extended to relatively large Stokes numbers of about 25, which was examined in the present study.

An analysis similar to the above was performed to investigate the joint characteristic of droplets and voids. Figure 28 presents the $JPDF$ of the voids normalized area ($A_v/\overline{A_v}$) versus the mean diameter of droplets within the voids (\tilde{d}'). Similar to Fig. 26, the first to fifth columns correspond to the no co-flow, $U = 3.5, 7.0, 10.5,$ and 14.0 m/s, respectively. Also, the results in the first to third columns pertain to the first to third turbulence generation mechanisms, respectively. The results presented in Fig. 28 show that the presence of the co-flow (compared to the no co-flow condition) increases the probability of relatively large droplets to reside within the voids. The results in the second to fifth columns of Fig. 28 suggest that increasing the mean bulk flow velocity and changing the turbulence generation mechanisms do not substantially change $JPDF(A_v/\overline{A_v}, \tilde{d}')$. This suggests that the turbulent co-flow may not facilitate positioning of the droplets within the voids.

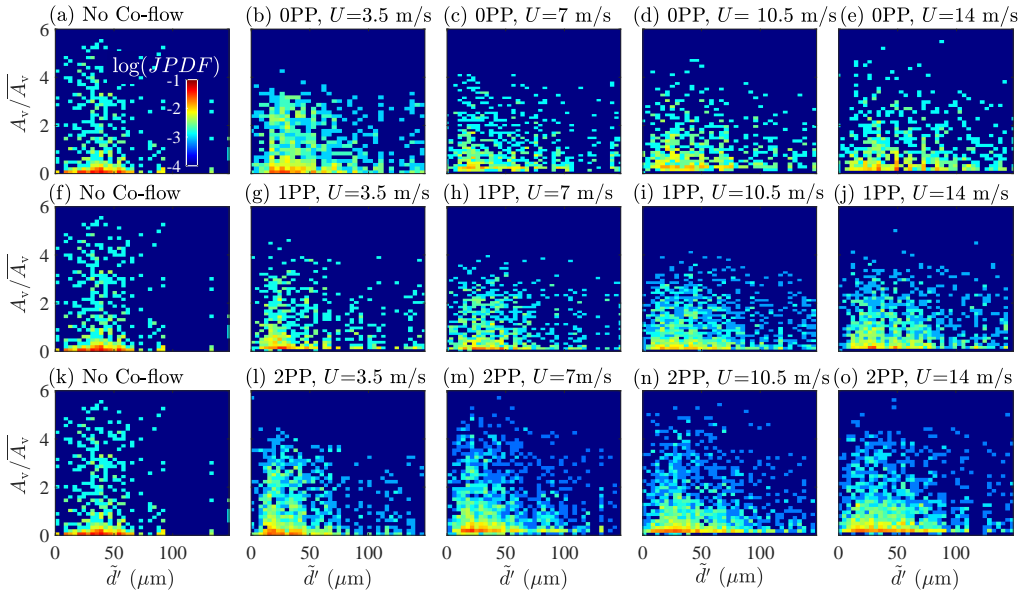


Figure 28. The logarithmic joint probability density function of the normalized area of the voids ($A_v/\overline{A_v}$) and the mean diameter of the droplets that exist within the voids ($\overline{d'}$). The first column corresponds to the no co-flow test condition and is repeating in each row for comparison purposes. The second to fifth columns correspond to the mean bulk flow velocities of 3.5, 7.0, 10.5, and 14.0 m/s, respectively. (b–e), (g–j), and (l–o) present the results for the first to third turbulence generation mechanisms, respectively.

5. Concluding remarks

Separate and joint characteristics of droplets diameter and clusters/voids size at relatively large Stokes numbers were investigated experimentally. Simultaneous Mie scattering and Interferometric Laser Imaging for Droplet Sizing (ILIDS) were performed to acquire the spatial distribution of the droplets and their corresponding diameters. Also, separate hotwire anemometry was performed to characterize the background turbulent flow. A flow apparatus was utilized to produce a water spray injected in a turbulent co-flow of air. Mean bulk flow velocities of 0 (no co-flow), 3.5, 7.0, 10.5, and 14.0 m/s were examined. Three turbulence generation mechanisms (zero, one, and two perforated plates) were used in the present study. The above mean bulk flow velocities and turbulence generation mechanisms allowed to vary the Kolmogorov time scale-based Stokes number and Taylor length scale-based Reynolds number from 3 to 25 as well as 10 to 38, which correspond to relatively large and moderate values (compared to those reported in the literature), respectively. The volume fraction of the spray was varied from about 10^{-6} to 2×10^{-6} , which rendered the tested sprays as dilute.

The Voronoï analysis was performed to calculate the degree of clustering as well as to identify the clusters and voids. The results showed that, for the test conditions that one perforated plate was used, the addition of the co-flow to the spray increases the degree of clustering. However, for test conditions with one and two perforated plate(s), the addition of the co-flow decreases the degree of clustering. The results of the present study and those of past investigations were compiled, and it was obtained that the degree of clustering is primarily influenced by the Stokes number. Specifically, increasing this number from zero to about 5 increases the degree of clustering from zero to about 1.2; however, for test conditions with Stokes numbers larger than about 5, the degree of clustering does not depend remarkably on the Stokes number and plateaus at about 0.7–1.

The clusters centers of areas were obtained and the corresponding Voronoi cells were formed for all test conditions. The results showed that the probability density function of these cells area normalized by their corresponding mean collapse on that of the Random Poisson Process; and, as a result, the clustering of the clusters does not occur for conditions tested here. The mean locations of the clusters and voids were obtained, and it was shown that while the former is located near the core of the spray, the latter is positioned at periphery of the spray. It was shown that, at a fixed Taylor length scale-based Reynolds number, increasing the Stokes number stretches the clusters location along the jet centerline, facilitating their existence at farther distances from the spray. However, at a fixed Stokes number, increasing the Taylor length scale-based Reynolds number shrinks the region where clusters exist along the jet centerline.

The length scales of the clusters and voids were estimated and compared with those of the background turbulent co-flow. The results showed that the mean void length scale was on the order of the integral length scale for all test conditions. However, the mean cluster length scale is smaller than the integral length scale but larger than the Taylor length scale. It was shown that increasing the Stokes number increases the mean cluster length scale to about 60 times the Kolmogorov length scale.

The results showed that the number density of the droplets within the clusters is about one order of magnitude larger than that for the voids, and both number densities decrease and then plateau with increasing the Stokes and Taylor length scale-based Reynolds numbers. It was obtained that the ratios of the clusters and voids number densities to the total number density of the spray are independent of the test conditions and nearly equal 8.3 and 0.7, respectively. The joint probability density function analysis was utilized to study the joint characteristics of the droplets and clusters/voids. It was concluded that a relatively wide range of cluster length scales can accommodate the most probable droplet diameter (about $30\ \mu\text{m}$) for all test conditions. It was shown that, although the joint PDF of the droplets diameter was not noticeably sensitive to the co-flow, increasing the Stokes and Taylor length scale-based Reynolds numbers increase the possibility of residing large droplets within the clusters. This was explained to be linked to increased range of eddy sizes interacting with droplets due to the increase of the above non-dimensional parameters.

Acknowledgments

The authors are grateful for the financial support from The University of British Columbia through the Eminence Fund program. Sina Kheirkhah acknowledges the financial support from the Canada Foundation for Innovation.

Declaration of interest

The authors report no conflict of interest.

Appendix A: Spray volume flow rate calibration

For the spray volume flow rate (\dot{Q}) calibration, first, the spray injector shown in Fig. 2 was connected to a sealed container; and then, the upstream pressure of the injector (P_v) was set to several values ranging from about 50 to 800 kPa using the pressure controller shown as item (2) in Fig. 1. For each set value of the upstream pressure, a high-precision scale was used to measure the collected water mass, which was converted to volume by using the water density at the laboratory temperature of 20°C . Then, the volume flow rate was calculated by dividing the volume of the collected water (in liters) to the time duration of

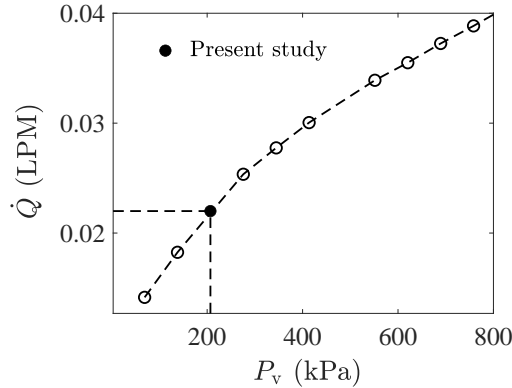


Figure 29. Calibration relation between the water vessel pressure and the spray flow rate.

the calibration experiment, which was 120 s. Figure 29 presents the variation of \dot{Q} versus P_v . For all conditions tested in the present study, P_v was set to 206 kPa, which led to a spray volume flow rate of 22 cubic centimeter per minute (see the black circular data symbol in Fig. 29).

Appendix B: Procedure for registering the Mie scattering images to the ILIDS images

The centers of the droplets identified from the ILIDS images are not identical to those obtained from the Mie Scattering images, and a discrepancy exists between the centers of the droplets identified from the above diagnostics. In addition to the present study, such discrepancy is also noted and discussed in the past investigations, see for example Boddapati *et al.* (2020) and Hardalupas *et al.* (2010). For the droplets and clusters/voids joint characteristics calculations, it is important to remove the discrepancy between the centers of the droplets obtained from the Mie scattering and ILIDS images. The procedure for removing the above discrepancy and thus registering the Mie scattering to the ILIDS images is discussed in the following.

First, a 2D target plate was manufactured and positioned in the location illuminated by the laser sheet in the experiments. Then, the images of the target plate were captured by the cameras used for collecting the Mie scattering and ILIDS images, with the collected images shown in Figs. 30(a) and (b), respectively. Eighteen points, see the green circles in Fig. 30(a), were considered and were identified in Fig. 30(b). The collective geometrical shape of these points was purposely selected to be asymmetric, facilitating the above identification. Then, the matrix that transforms data points in Fig. 30(a) to those in Fig. 30(b) was obtained. This transformation matrix was used for registering the Mie scattering images to the ILIDS images, with a representative result for such transformation discussed below.

A representative and simultaneously acquired Mie scattering and ILIDS images are shown in Figs. 31(a) and (b), respectively. The results correspond to the test condition with one perforated plate and the mean bulk flow velocity of 10.5 m/s. Figure 31(c) presents the results in Fig. 31(a) after the application of the above transformation. Figure 31(d) presents that in Fig. 31(b) after application of the convolution discussed in subsection 3.2. The procedure discussed in subsection 3.2 was followed to identify the centers of the droplets from the results shown in Fig. 31(d), with the corresponding centers shown by the blue circular data points in Fig. 31(e). Overlaid on Fig. 31(e) are also the centers of the droplets obtained from binarizing the Mie scattering image in Fig. 31(c). The centers of the droplets obtained from

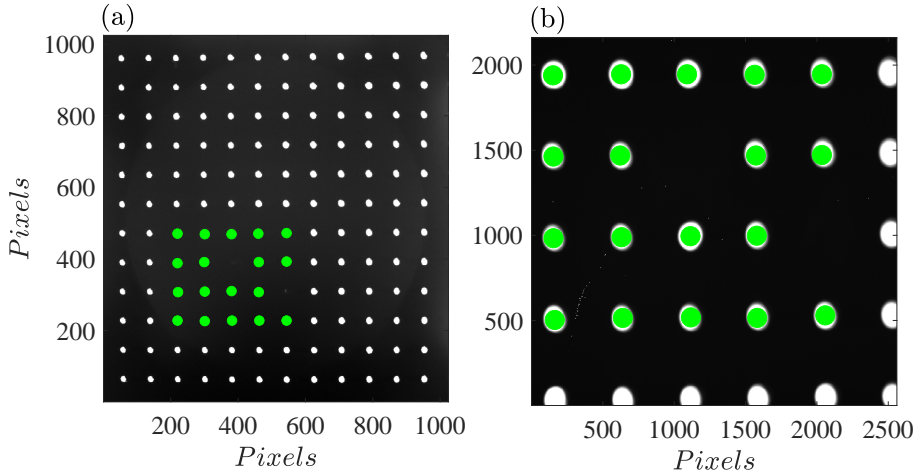


Figure 30. (a) and (b) are the images of the target plate captured by the Mie Scattering and ILIDS cameras, respectively.

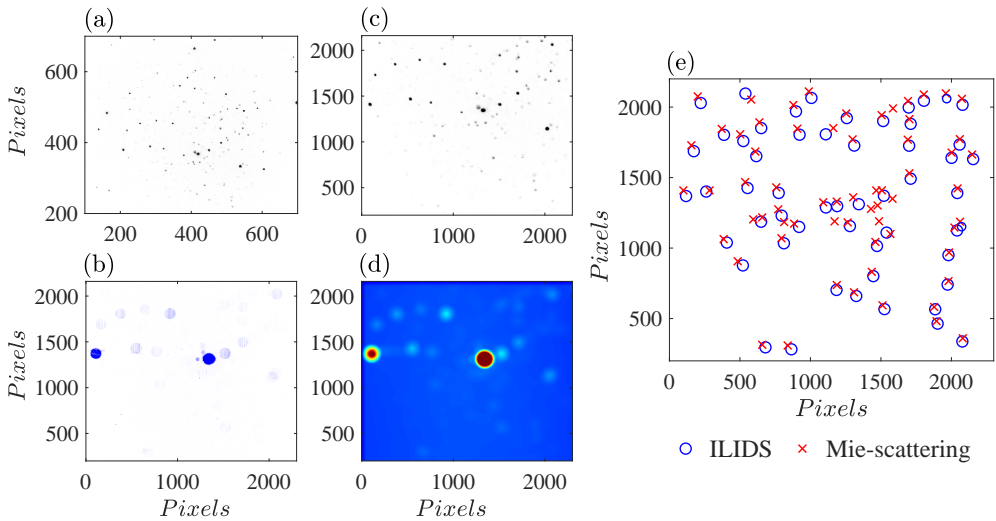


Figure 31. (a) and (b) are representative raw Mie scattering and ILIDS images, respectively. (c) is the image obtained by mapping that shown in (a) to the imaging plane of the ILIDS camera. (d) is the convolution of the results shown in (b) with a disk-shaped mask. (e) presents the centers of the droplets obtained from the ILIDS and Mie scattering images.

the Mie scattering image are shown by the red cross data symbols in Fig. 31(e). As can be seen, the spatial locations of the blue circular data symbol are close to those of the red cross data symbol. Thus, for calculating the joint characteristics of the droplets and clusters (voids), the centers identified from the ILIDS image were replaced by those obtained from the Mie scattering image.

REFERENCES

AKAMATSU, FUMITERU, MIUTANI, YUKIO, KATSUKI, MASASHI, TSUSHIMA, SHOHJI & CHO, YONG DAE 1996

- Measurement of the local group combustion number of droplet clusters in a premixed spray stream. *Proc. Combust. Inst.* **26** (1), 1723–1729.
- ALISEDA, ALBERTO, CARTELLIER, ALAIN, HAINAUX, F & LASHERAS, JUAN C 2002 Effect of preferential concentration on the settling velocity of heavy particles in homogeneous isotropic turbulence. *J. Fluid Mech.* **468**, 77–105.
- ANDRADE, PAUL, HARDALUPAS, YANNIS & CHARALAMPOUS, GEORGIOS 2022 Study of preferential concentration in turbulent flows using combined graph theory and Voronoï analysis. *Phys. Fluids* **34** (5), 051704.
- BAKER, LUCIA, FRANKEL, ARI, MANI, ALI & COLETTI, FILIPPO 2017 Coherent clusters of inertial particles in homogeneous turbulence. *J. Fluid Mech.* **833**, 364–398.
- BALACHANDAR, S & EATON, JOHN K 2010 Turbulent dispersed multiphase flow. *Annu. Rev. Fluid Mech.* **42**, 111–133.
- BOCANEGRA EVANS, HUMBERTO, DAM, NICO, VAN DER VOORT, DENNIS, BERTENS, GUUS & VAN DE WATER, WILLEM 2015 Measuring droplet size distributions from overlapping interferometric particle images. *Rev. Sci. Instrum.* **86** (2), 023709.
- BODDAPATI, VIVEK, MANISH, M & SAHU, SRIKRISHNA 2020 A novel approach for conditional measurement of droplet size distribution within droplet clusters in sprays. *Exp. Fluids* **61** (2), 1–17.
- BRANDT, LUCA & COLETTI, FILIPPO 2022 Particle-laden turbulence: Progress and perspectives. *Annu. Rev. Fluid Mech.* **54**, 159–189.
- CROWE, CLAYTON, T, SCHWARZKOPF, JOHN, D, SOMMERFELD, MARTIN & TSUJI, YUTAKA. 2011 *Multiphase Flows with Droplets and Particles*. CRC Press.
- ELGHOBASHI, SAID 1994 On predicting particle-laden turbulent flows. *Appl. Sci. Res.* **52** (4), 309–329.
- FERENC, JÁRAI-SZABÓ & NÉDA, ZOLTÁN 2007 On the size distribution of Poisson Voronoi cells. *Physica A* **385** (2), 518–526.
- FESSLER, JOHN R, KULICK, JONATHAN D & EATON, JOHN K 1994 Preferential concentration of heavy particles in a turbulent channel flow. *Phys. Fluids* **6** (11), 3742–3749.
- FRANKEL, ARI, POURANSARI, HADI, COLETTI, FILIPPO & MANI, ALI 2016 Settling of heated particles in homogeneous turbulence. *J. Fluid Mech.* **792**, 869–893.
- GARCIA-MAGARINO, A, SOR, S, BARDERA, R & MUNOZ-CAMPILLEJO, J 2021 Interferometric laser imaging for droplet sizing method for long range measurements. *Measurement* **168**, 108418.
- GOTO, SUSUMU & VASSILICOS, JC 2006 Self-similar clustering of inertial particles and zero-acceleration points in fully developed two-dimensional turbulence. *Phys. Fluids* **18** (11), 115103.
- GOTO, SUSUMU & VASSILICOS, JC 2008 Sweep-stick mechanism of heavy particle clustering in fluid turbulence. *Phys. Rev. Lett.* **100** (5), 054503.
- HARDALUPAS, YANNIS, SAHU, SRIKRISHNA, TAYLOR, ALEX MKP & ZAROGULIDIS, KONSTANTINOS 2010 Simultaneous planar measurement of droplet velocity and size with gas phase velocities in a spray by combined ILIDS and PIV techniques. *Exp. Fluids* **49** (2), 417–434.
- HARDALUPAS, YANNIS, TAYLOR, ALEX MKP & WHITELAW, JAMES HUNTER 1994 Mass flux, mass fraction and concentration of liquid fuel in a swirl-stabilized flame. *Int. J. Multiphas. Flow* **20**, 233–259.
- HASSAINI, ROUMAÏSSA & COLETTI, FILIPPO 2022 Scale-to-scale turbulence modification by small settling particles. *J. Fluid Mech.* **949**, A30.
- HAYASHI, KENTARO, ICHIYANAGI, MITSUHIRA & HISHIDA, KOICHI 2012 Measurements of droplets spatial distribution in spray by combining focus and defocus images. *Exp. Fluids* **49**, 417–434.
- JEDELSKY, JAN, MALY, MILAN, DEL CORRAL, NOÉ PINTO, WIGLEY, GRAHAM, JANACKOVA, LADA & JICHA, MIROSLAV 2018 Air–liquid interactions in a pressure-swirl spray. *Int. J. Heat Mass Tran.* **121**, 788–804.
- KHEIRKHAH, SINA 2016 Experimental study of turbulent premixed combustion in V-shaped flames. PhD thesis, University of Toronto (Canada).
- KHEIRKHAH, SINA & GÜLDER, ÖMER L. 2014 Topology and brush thickness of turbulent premixed V-shaped flames. *Flow Turbul. Combust.* **93** (3), 439–459.
- KHEIRKHAH, SINA & GÜLDER, ÖMER L 2015 Consumption speed and burning velocity in counter-gradient and gradient diffusion regimes of turbulent premixed combustion. *Combust. Flame* **162** (4), 1422–1439.
- KUERTEN, J. G. M. 2016 Point-particle and LES of particle-laden turbulent flow—a state-of-the-art review. *Flow Turbul. Combust.* **97** (3), 689–713.
- MAXEY, MARTIN R 1987 The gravitational settling of aerosol particles in homogeneous turbulence and random flow fields. *J. Fluid Mech.* **174**, 441–465.

- MOHAMMADNEJAD, SAJJAD, SACA, LESLIE & KHEIRKHAH, SINA 2022 A new compact active turbulence generator for premixed combustion: Non-reacting flow characteristics. *Phys. Fluids* **34** (10), 105102.
- MONCHAUX, ROMAIN, BOURGOIN, MICKAËL & CARTELLIER, ALAIN 2010 Preferential concentration of heavy particles: A Voronoï analysis. *Phys. Fluids* **22** (10), 103304.
- MONCHAUX, ROMAIN, BOURGOIN, MICKAËL & CARTELLIER, ALAIN 2012 Analyzing preferential concentration and clustering of inertial particles in turbulence. *Int. J. Multiphas. Flow* **40**, 1–18.
- MORA, DO, BOURGOIN, MICKAËL, MININNI, PD & OBLIGADO, M 2021 Clustering of vector nulls in homogeneous isotropic turbulence. *Phys. Rev. Fluids* **6** (2), 024609.
- OBLIGADO, MARTIN, TEITELBAUM, TOMAS, CARTELLIER, ALAIN, MININNI, PABLO & BOURGOIN, MICKAËL 2014 Preferential concentration of heavy particles in turbulence. *J. Turbul.* **15** (5), 293–310.
- PANDURANGAN, NANDHAKUMAR & SAHU, SRIKRISHNA 2022 Spatial evolution of multi-scale droplet clusters in an evaporating spray. *Phys. Fluids* **34** (11), 113310.
- PETERSEN, ALEC J, BAKER, LUCIA & COLETTI, FILIPPO 2019 Experimental study of inertial particles clustering and settling in homogeneous turbulence. *J. Fluid Mech.* **864**, 925–970.
- PETRY, NIKLAS, SCHÄFER, DOMINIK, LAMMEL, OLIVER & HAMPP, FABIAN 2022 Quantification of coflow effects on primary atomization of pressure swirl atomizers. *Int. J. Multiphas. Flow* **149**, 103946.
- POELMA, CHRISTIAN & OOMS, GIJS 2006 Particle-turbulence interaction in a homogeneous, isotropic turbulent suspension. *Appl. Mech. Rev.* **59** (2), 78.
- QIENI, LU, KAN, HAN, BAOZHEN, GE & XIANG, WANG 2016 High-accuracy simultaneous measurement of particle size and location using interferometric out-of-focus imaging. *Opt. Express* **24** (15), 16530–16543.
- READE, WALTER C & COLLINS, LANCE R 2000 Effect of preferential concentration on turbulent collision rates. *Phys. Fluids* **12** (10), 2530–2540.
- SAHU, SRIKRISHNA, HARDALUPAS, YANNIS & TAYLOR, ALEX MKP 2016 Droplet–turbulence interaction in a confined polydispersed spray: effect of turbulence on droplet dispersion. *J. Fluid Mech.* **794**, 267–309.
- SAHU, SRIKRISHNA, HARDALUPAS, YANNIS & TAYLOR, ALEX MKP 2018 Interaction of droplet dispersion and evaporation in a polydispersed spray. *J. Fluid Mech.* **846**, 37–81.
- SALAZAR, JUAN PLC, DE JONG, JEREMY, CAO, LUJIE, WOODWARD, SCOTT H, MENG, HUI & COLLINS, LANCE R 2008 Experimental and numerical investigation of inertial particle clustering in isotropic turbulence. *J. Fluid Mech.* **600**, 245–256.
- SAW, EWE WEI, SHAW, RAYMOND A, AYYALASOMAYAJULA, SATHYANARAYANA, CHUANG, PATRICK Y & GYLFASSON, ARMANN 2008 Inertial clustering of particles in high-Reynolds-number turbulence. *Phys. Rev. Lett.* **100** (21), 214501.
- SQUIRES, KYLE D & EATON, JOHN K 1991 Preferential concentration of particles by turbulence. *Phys. Fluids* **3** (5), 1169–1178.
- SUMBEKOVA, SHOLPAN, CARTELLIER, ALAIN, ALISEDA, ALBERTO & BOURGOIN, MICKAËL 2017 Preferential concentration of inertial sub-Kolmogorov particles: the roles of mass loading of particles, Stokes numbers, and Reynolds numbers. *Phys. Rev. Fluids* **2** (2), 024302.
- TAGAWA, YOSHIYUKI, MERCADO, JULIÁN MARTÍNEZ, PRAKASH, VIVEK N, CALZAVARINI, ENRICO, SUN, CHAO & LOHSE, DETLEF 2012 Three-dimensional Lagrangian Voronoï analysis for clustering of particles and bubbles in turbulence. *J. Fluid Mech.* **693**, 201–215.
- TAYLOR, GEOFFREY INGRAM 1938 The spectrum of turbulence. *Proc. R. Soc. Lon. Ser-A* **164** (919), 476–490.
- THIMOTHÉE, ROMAIN, CHAUVEAU, CHRISTIAN, HALTER, FABIEN & GÖKALP, ISKENDER 2016 Experimental investigation of the presence of fuel droplets after the passage of a flame front. In *27th European Conference on Liquid Atomization and Spray Systems*.
- VILLAFANE-ROCA, LAURA, ESMAILY-MOGHADAM, M, BANKO, A & EATON, JK 2016 A robust method for quantification of preferential concentration from finite number of particles. *Center for Turbulence Research Annual Research Briefs* pp. 123–135.
- WANG, JINHUA, YU, QIANQIAN, ZHANG, WEIJIE, ZHANG, MENG & HUANG, ZUOHUA 2019 Development of a turbulence scale controllable burner and turbulent flame structure analysis. *Exp. Therm. Fluid Sci.* **109**, 109898.
- WANG, LIAN-PING & MAXEY, MARTIN R 1993 Settling velocity and concentration distribution of heavy particles in homogeneous isotropic turbulence. *J. Fluid Mech.* **256**, 27–68.
- WANG, XIANGJUN, WAN, MINPING, YANG, YAN, WANG, LIAN-PING & CHEN, SHIYI 2020 Reynolds number dependence of heavy particles clustering in homogeneous isotropic turbulence. *Phys. Rev. Fluids* **5** (12), 124603.

- YANG, TS & SHY, SS 2005 Two-way interaction between solid particles and homogeneous air turbulence: particle settling rate and turbulence modification measurements. *J. Fluid Mech.* **526**, 171–216.
- YOSHIMOTO, HIROSHI & GOTO, SUSUMU 2007 Self-similar clustering of inertial particles in homogeneous turbulence. *J. Fluid Mech.* **577**, 275–286.
- ZHAO, RUI-JIE, ZHAO, YOU-LONG, ZHANG, DE-SHENG, LI, YAN & GENG, LIN-LIN 2021 Numerical investigation of the characteristics of erosion in a centrifugal pump for transporting dilute particle-laden flows. *J. Mar. Sci. Eng.* **9** (9), 961.
- ZIMMER, LAURENT, DOMANN, ROLAND, HARDALUPAS, YANNIS & IKEDA, YUJI 2003 Simultaneous laser-induced fluorescence and Mie scattering for droplet cluster measurements. *AIAA* **41** (11), 2170–2178.